ABSTRACT

MECHANICS OF BINDER-PARTICLE INTERACTIONS IN COMPOSITE BATTERY ELECTRODES

by
Richard Johnson

A study into the particle level mechanics of polymer binder and active material used in composite lithium-ion batteries (LIB) has been conducted. Silicon is highly sought after material that can be used as an active material in a composite anode. Its high theoretical capacity can result in batteries that can store more energy than current LIBs, but high volume expansion of Si during charge/discharge cycles leads to rapid capacity fade and poor cyclic life. Understanding the stress that is generated in the binder and the active material due to the volume expansion has not been fully understood. In this study an idealized composite electrode sample was created to emulate the binder/particle interactions in a commercial composite electrode. The sample was fabricated by etching micro pillars of Si into a crystal Si wafer in a periodic array. Polyvinylidene fluoride (PVDF) and sodium carboxymethyl cellulose (CMC) were then added to the system to form binder bridges between Si pillars. The stress induced in this composite electrode during electrochemical cycling was measured in situ using a multi-beam optical sensor (MOS). A preliminary finite element model was generated which can be used to interpret the stress at the binder/particle interface.

During electrochemical cycling the liquid electrolyte in the LIB reacts with the active particles to form a passivation layer called solid electrolyte interphase (SEI) layer on the electrode surfaces. The location and composition of the SEI can influence the interface properties between binder and active particles which will influence the overall cyclic performance of batteries. However, the effect of binder on the SEI formation has not been fully realized. To understand the effect of binder on the location of the SEI, thin films of PVDF and CMC were spin coated onto crystal Si

wafers. The wafers were then cycled to grow a stable SEI layer. X-ray photoelectron spectroscopy (XPS) coupled with depth profile analysis using C-60 ion sputtering was then conducted to analyze the composition of SEI as well as the location of the SEI compounds within the binder. The depth profiling data revealed that SEI forms within the binder but not on the outer layer of the binder. These results can help inform the optimization of Si containing anodes in commercial LIB.

MECHANICS OF BINDER-PARTICLE INTERACTIONS IN COMPOSITE BATTERY ELECTRODES

by
Richard Johnson

A Thesis
Submitted to the Faculty of
New Jersey Institute of Technology
in Partial Fulfillment of the Requirements for the Degree of
Master of Science in Mechanical Engineering

Department of Mechanical and Industrial Engineering

May 2019

APPROVAL PAGE

MECHANICS OF BINDER-PARTICLE INTERACTIONS IN COMPOSITE BATTERY ELECTRODES

Richard Johnson

Dr. Siva P. Nadimpalli, Dissertation Advisor — Date
Associate Professor of Mechanical and Industrial Engineering, NJIT

Dr. Joga Rao , Committee Member — Date
Professor and Chair of Mechanical and Industrial Engineering,, NJIT

Dr. Shawn A. Chester,, Committee Member — Date
Assistant Professor of Mechanical and Industrial Engineering, NJIT

BIOGRAPHICAL SKETCH

Author: Richard Johnson

Degree: Master of Science

Date: May 2019

Undergraduate and Graduate Education:

- Master of Science in Mechanical Engineering,
  New Jersey Institute of Technology, Newark, NJ, 2019
- Bachelor of Science in Mechanical Engineering,,
  New Jersey Institute of Technology, Newark, NJ, 2016

Major: Mechanical Engineering

Presentations and Publications:

Patrick B.Thompson, RichardJohnson, Siva P.V.Nadimpalli, "Effect of temperature on the fracture behavior of Cu/SAC305/Cu solder joints," *Engineering Fracture Mechanics*, vol. 199, 730-738, August 2018

I would like to thank everyone who has ever supported me, I would never have been able to achieve anything without you.

ACKNOWLEDGMENT

I would like to thank my advisor Dr. Siva Nadimpalli for all of his help and continued support. I would like to also thank both Dr. Gordon Waller and Dr. Azzam Mansour for their tireless efforts in helping me understand the principles of both electrochemistry and XPS analysis. I would like to thank my committee members Dr. Joga Rao and Dr. Shawn Chester for their feedback and questions, which helped me to get a new perspective on the many aspects of this thesis. I would like to thank Maria Medeiros and the Office of Naval Research(Award Number: N00014-17-1-2345) for their financial support of this project. Finally I would like to thank all my colleagues in the Mechanical Engineering Department including Akshay Pakhare, Subhajit Rakshit, and Igor Bezsonov for their help with sample fabrication and their help with any questions I had. Thank you all.

TABLE OF CONTENTS

TABLE OF CONTENTS
(Continued)

Chapter **Page**

LIST OF TABLES

LIST OF FIGURES

LIST OF FIGURES
(Continued)

Figure **Page**

CHAPTER 1

INTRODUCTION

1.1 Motivation

The use of unmanned vehicles is of high interest to the United States Navy. This interest arose in 1994 when the Navy identified an immediate need for a form of anti-mine countermeasures to integrate into submarines. Unmanned undersea vehicles (UUV) were found to be the perfect system to implement and thus a major focus was placed on their development and implementation. Six major tasks were then highlighted for these vehicles to take on. They were surveillance and reconnaissance, mine countermeasures, anti-submarine warfare, inspection/identification, oceanography, and payload delivery. A key advantage UUVs hold over submarines is that, due to their variable size, they are capable of surveying shallow water[7].

In order to supply power to UUVs there are many options such as primary batteries, rechargeable batteries, fuel cells, and hybrid systems containing multiple forms of energy storage devices. Of these options, rechargeable lithium-ion batteries (LIB) provide excellent current density and, unlike primary LIBs, they do not need to be removed and replaced after their use. They also hold an advantage over fuel cells in that no port holes are needed to supply more fuel to the UUV only a simple charging port is needed to resupply the UUV with energy [6].

In order to keep a technological advantage over other countries there is a need to improve upon the operational endurance of UUVs. The operational endurance describes the maneuverability, the efficiency, and the resiliency for sustained operations of a specific platform. To improve upon these key objectives the energy storage and energy efficiency must be improved for the propulsion system, weapon system, and sensors utilized by the UUVs. An improvement in operational

efficiency will lead to a more agile and efficient UUV, while also increasing total mission duration[6]

Another key area of improvement for UUV technology is the reduction of the size of the energy storage system. By reducing the size of the energy storage system there can be more volume within the UUV that can be dedicated to more sensing equipment[6]. A challenge is made clear where there is a desire to improve upon the performance of the energy storage system, while also reducing its size. In order to meet these design parameters high energy density materials must be implemented into LIBs. One key high energy density material is silicon, which has the capability of outperforming current battery technology. The following section will provide a background on LIBs in order to further explain how high energy density martials like Si can be implemented, as well as, the key challenges that hinder their immediate use.

1.2 Background Information: LIB

LIBs have the highest energy density when compared to other rechargeable batteries making them the most popular energy storage device used in portable electronics as well as electric vehicles[28]. LIBs are also capable of operating at a wide range of temperatures (25 to 50°) which will allow for their utilization in any undersea environment. The schematic in Figure 1.1 highlights the basic components of a LIB. The major components are the electrodes, the liquid electrolyte, and the polymer separator. The anode is the negative electrode associated with the release of electrons into the external circuit and the cathode is the positive electrode associated with the gain of electrons from the external circuit. The liquid electrolyte between the two electrodes consists of a solution of Li-salts dissolved in an organic solvent. The electrolyte is ionically conductive but electronically insulating and allows for the shuttling of Li-ions from the anode to the cathode as depicted in Figure 1.

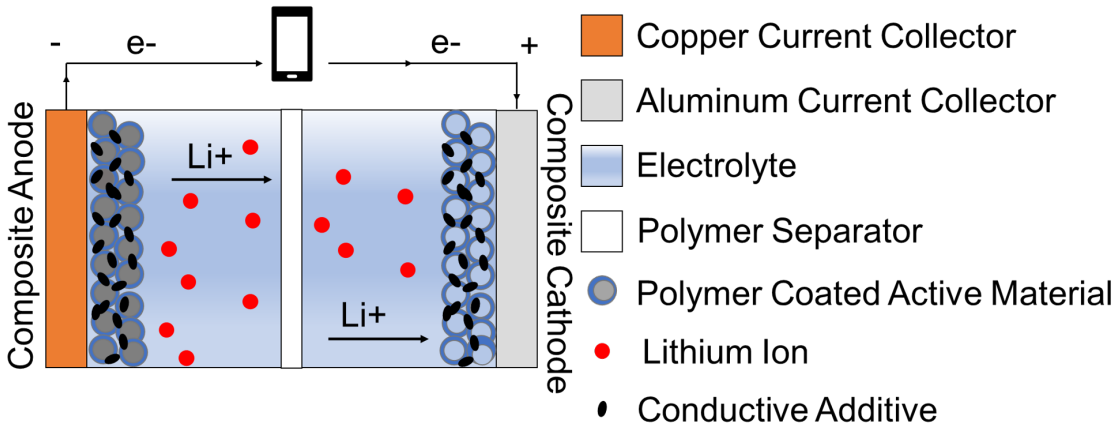

Figure 1.1 Schematic of a lithium-ion battery.

Between the two electrodes is a polymer separator depicted as a white barrier. The separator is a porous media which is also electronically insulating. The separator allows for the passage of ions between the two electrodes while preventing them from touching, which would cause failure of the battery[30].

Taking a closer look at the two electrodes it can be seen through Figure 1 that they are comprised of multiple components. These components are the current collector, active material, polymer binder, and conductive additives. Most commercial rechargeable LIBs are comprised of composite electrodes which is why they are the focus of this study. The current collectors used are typically copper for the anode and aluminum for the cathode and they help to create an external circuit. These two metals were chosen based on their incompatibility with Li at their respective operating potentials. The active material is depicted as grey circles in Figure 1.1. The active material is capable of reversibly reacting with Li in response to a voltage change in order to generate an electrical current by means of a chemical reaction. For typical commercial LIBs the active material in the anode is graphite, and the typical active material in the cathode is a transition metal oxide such as LiMnO2. The active material is then mixed with a conductive additive and adhered to the current collector using a polymer binder. The binder used plays an important role

in creating a cohesive matrix of active material and conductive additive, while also adhering that matrix to the current collector. The result is an electrical network of active material connect to the current collector.

LIBs function by shuttling charge carrying Li-ions from the anode to the cathode. As the battery is discharged Li+ ions are released from the anode in an oxidized state. They then pass through the electrolyte and into the cathode where they are then be reduced and intercalated in to the cathode's active material. Intercalation is the insertion and extraction of Li into the crystal structure of the active material. During charging the reverse reaction occurs in which the Li-ions are intercalated into the graphite in the anode. As Li-ions travel between the two electrodes, an electrical current flow from the current collectors through an external circuit.

In order to improve upon the performance and efficiency of LIBs it is crucial to identify the key elements of the battery that have the highest impact on the overall performance. The two components that influence the performance to the highest degree are the active material and the electrolyte. In this study the focus will be placed on the active material. The active material plays a vital role in dictating the energy density and cyclic life of the LIB. In order to achieve higher energy density, the active material must be replaced with a high energy density material such as Si[20].

1.3 Stress Development Inside Composite Electrodes

Unlike graphite, Li does not intercalate into Si. Si undergoes a conversion reaction in which crystalline Si becomes amorphous Si during the process of electrochemical cycling. This process breaks the bonds between the Si atoms and results in large volumetric expansion. It also allows for a higher concentration of Li to be added to the Si when compared to an intercalation reaction. The theoretical capacity for Si is 4200 mAhg-1 while the theoretical capacity for graphite is 372 mAhg-1.

Although the theoretical capacity of Si is an order of magnitude higher than graphite there is one major issue that has prevented its implantation into LIBs. As previously mentioned, the alloying/dealloying reaction of Li with Si results in large volume expansion of the Si due to a crystalline to amorphous phase transformation. This volume expansion can be up to 300% the original volume, which causes high stress. The result is fracture and pulverization of the Si particles as the battery cycles. When these particles fracture, they are removed from the electrical network and become electronically isolated. This leads to rapid capacity fading, which is the irreversible loss of capacity. Capacity fade in turn results in poor cyclic life, and it is the major hindrance towards Si's implementation into commercial LIBs.

As seen in Figure 1.1, a single particle of active material is constrained by the neighboring particles as well as the current collector. The effect of these constraints leads to most of the stress inside the composite anode. During cycling there exists a gradient of Li concentration from the outer surface of a particle of Si to its core. This can imply that at any point in the electrochemical cycle, or state of charge, the Si can have different phases existing at once all with different material properties. As previously stated, the constraints imposed by neighboring particles in a composite electrode contribute to a majority of stresses, therefore this phenomenon is of key interest.

At the particle level it can be seen through Figure 3.1 that between neighboring particles of Si in a composite anode, binder bridges are formed[25]. These binder bridges help to create the electrical network of the electrode and thus, failure of these bridges leads to capacity fade and poor cyclic life. A fundamental understanding of the stress which are generated during cycling within the binder at the particle level has not been fully explored. In recent studies, the real-time stress experienced within the composite film was measured through an optical curvature measurement. This was done by utilizing a multi-beam optical

sensor (MOS) to track the change in curvature within the composite film.

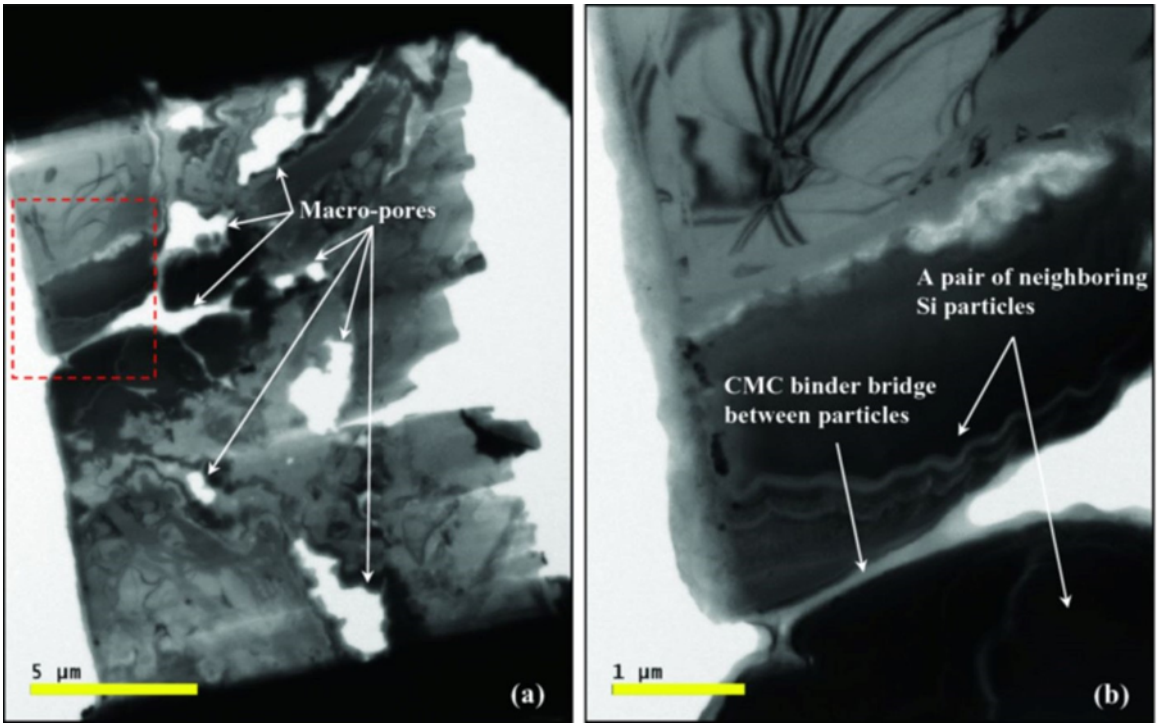

Figure 1.2 Transmission electron microscopy (TEM) image of a thin slice (ca. 300 nm thick) prepared via FIB cross-section of a partially lithiated Si/CMC composite electrode.

Source: Sethuraman, V. A., Nguyen, A., Chon, M. J., Nadimpalli, S. P. V., Wang, H., Abraham, D. P., ... Guduru, P. R. (2013). Stress Evolution in Composite Silicon Electrodes during Lithiation/Delithiation. Journal of The Electrochemical Society, 160(4), A739–A746.

However, this methodology was only capable of interpreting the averaged stress experienced throughout the film. This study aims to further the understanding of the stresses developed at the particle level by creating an idealized composite anode sample specifically designed to measure stress. This information will help to create a finite element model of the binder/active material such that the stresses at the interface can be interpreted. The information gained from this model can help in the optimization of Si containing anode in commercial LIBs.

1.4 Background Information: Solid Electrolyte Interphase Layer

Although the stress and subsequent fracture and pulverization of Si is the leading cause of capacity fade, there is another phenomenon that exist which exacerbates the irreversible capacity loss. That phenomenon is the growth of the solid electrolyte interphase (SEI) layer. The SEI consists of a very thin (10 nm) layer of multiple organic and inorganic compounds. This layer is formed instantaneously as a negative potential is applied to Si. It forms as both the salt and solvent in the electrolyte are reduced on the surface of the Si due to the thermodynamic instability of the electrolyte at the low potentials in which the anode operates. The formation of this layer consumes Li from the system and thus results in an irreversible capacity fade. Despite the irreversible loss of Li, the SEI is essential for the successful operation of rechargeable LIBs. This is because the SEI is a passivating layer which has high electronic resistance; therefore, it acts as a protective layer around the Si by preventing the electrolyte from being constantly reduced during the life cycle of the LIB. The layer is formed predominantly during the first cycle and the thickness of the layer is determined by the range of electron tunneling. Once electron tunneling can no longer occur the layer will no longer grow, and no more Li will be consumed.

The issue with the SEI formed is Si based anodes is that the volume expansion which occurs during cycling is so great that the SEI is cracked. During this process fresh Si is exposed, which then begins to react with the electrolyte forming a new layer of SEI. Over multiple cycles the SEI layer continues to shed and thus unstable growth of a thick layer of SEI occurs. This unstable growth leads to continued consumption of the electrolyte and the Li resulting in capacity fade.

Furthermore, the effect the polymer binder has on the formation and location of the SEI has not been fully understood. As mentioned in the previous section, the key area of interest in a composite electrode is the interface between the binder and the active material. Favorable interface properties between the binder and the active

material is imperative for composite anodes that experience large stresses between particles. The location of the SEI can influence these properties and effect the adhesion between the binder and the active material, thus a better understanding of the location of the SEI within the binder is needed as well as the mechanisms that lead to SEI forming at different locations within the binder.

1.5 Objectives

The objective of this thesis is to fully understand the mechanics of the binder/active material interactions at a particle level. This objective will be carried out by first understanding the effect of binder on the location, as well as, the composition of the SEI formed during electrochemical cycling. Two polymers, polyvinylidene fluoride (PVDF) and sodium carboxymethylcellulose (CMC) will be considered in this study. Next an idealized composite anode will be fabricated in order to emulate the binder/active material interactions that occur in a standard composite electrode. This will be done by etching micro pillars into a crystal Si wafer. The pillars will be periodic in nature such that their geometry will be easy to model. A preliminary finite element model will then be created to interpret the stresses in the binder bridges between Si particles.

CHAPTER 2

X-RAY PHOTOELECTRON SPECTROSCOPY OF THE CYCLED BINDER COATED AND BARE SILICON ANODES

2.1 Background Information

As mentioned earlier, one of the main cause of poor cyclic life of LIBs is the failure of binder bridges between Si particles, as well as, the pulverization of Si particles in composite electrodes. It was observed that nanoscale Si particles resist pulverization of Si, and there exists a critical particle size (150 nm) below which fracture would not occur when Si is electrochemically cycled [15]. Although the nanoscale particles were more fracture resistant, they still had poor first cycle efficiency due to failure of binder bridges[29]. These reports have demonstrated that the binder plays a critical role in the successful functioning of composite electrodes.

Many different binders have been investigated to understand the effect of their properties such as adhesion to active particles and their ability to absorb electrolyte on the performance of composite electrodes. The chemical structure of the binders was also found to play a key role in the overall performance of the electrode[3] [13] [8] [17][14][19]. The most commonly studied binders are polyvinylidene fluoride (PVDF) and sodium carboxymethylcellulose (CMC). PVDF is a conventional binder material and it adheres to Si with weak van der Waals forces, while CMC is a linear polymeric derivative of cellulose that contains carboxylic functional groups, which can adhere to the surface of the Si[12]. Initially it was believed that the use of elastomeric binders such as PVDF would improve the performance of Si based anodes. However, Chen et al. and Li et al. found that the CMC/SBR outperformed the PVDF in terms of cyclic performance[4][13]. This result was unexpected since the PVDF was believed to have favorable mechanical properties. It was concluded that PVDF's ability to

absorb electrolyte was the cause for its poor performance[3]. The adhesion of the CMC to Si particles was attributed to its improved performance as stated by Li et al. and Key et al.[13][10] Bridel et al. investigated the proper ratio of Si / binder / conductive additive to understand the effect of binder content on electrochemical performance. It was found that a 1:1:1 ratio was the most optimal and the hydrogen bonds between the carboxy groups in CMC and the hydroxyl groups on the surface of the Si exhibit a self-healing behavior which helped to improve the performance of the CMC-based electrode[1].

Polyacrylic acid (PAA) is another promising binder alternative and it consists of carboxylic functional groups that bond to the hydroxyl groups on the Si surface[16]. Magasinski et al. compared the performance of PAA and CMC and showed that the PAA outperformed CMC due to the presence of relatively higher percentage of carboxylic groups which improved adhesion[16]. It was noted by Mazouzi et al. that the pH level of a binder solution greatly affects the cyclic performance[18]. For example, a CMC solution with a pH of 3 promoted better bonding between the CMC and the Si. An acid CMC solution was then compared to PAA by Karkar et al. where the performance of an acidic CMC was found to be comparable to PAA[9].

From the above, a key conclusion is that the adhesion and the binder's ability to swell with electrolyte are the key factors in determining the viability of the binder in the next generation composite anodes for LIBs. What is lacking in the literature is the understanding of the location of the SEI that is formed during electrochemical cycling within the binder. The location of the SEI can affect the adhesion. The binder's ability to swell with electrolyte may further influence the location of the SEI. In this study the effect the binder has on the location of SEI was studied using X-ray photoelectron spectroscopy (XPS). XPS can be used to characterize the chemical composition of the surface of the binder after cycling[22].

X-ray photoelectron spectroscopy (XPS) is a surface analysis technique that allows for the quantification of the elemental composition of a sample. XPS is also capable of determining the type of bonding and oxidation state of a sample based on the elemental signals that are recorded. This is possible due to the nature of the analysis technique. X-rays with know energy levels are utilized to excite the surface level electrons of the sample which get ejected from the sample. The ejected electrons are known as photoelectrons because they are emitted due to interactions with high energy photons. An electron energy analyzer is used to measure the energy of the emitted photoelectrons. The kinetic energy of the photoelectron leaving the sample is described by

$$KE = h\nu - (BE + \psi_{sample}) \tag{2.1}$$

Where KE is the kinetic energy of the emitted photoelectron, BE is the binding energy of the emitted photoelectron, h is Plank's constant, ν is the photon frequency (the speed of light divided by the photon wavelength), and ψ_{sample} is the work function of the sample.

The BE of an emitted photoelectron describes the energy needed to remove that electron from the surface of the sample. The BE of a photoelectron is influenced by the type of bonds that are present, as well as, the oxidation state of the compound the photoelectrons are emitted from. Thus, from the binding energy as well as the intensity of the corresponding photoelectron peaks, the quantity and composition of the sample's surface can be determined.

When analyzing the data from an insulating sample, such as a polymer, there is a need to correct the BE due to the charging of the specimen. As an insulating sample is bombarded with X-rays it begins to gain a positive charge which can cause

errors in the kinetic energy observed during analysis. Therefore, a charge correction is needed. Typically, the charge correction is done such that the peak with the lowest binding energy found in the carbon region of the sample is aligned with the known peak position of adventitious carbon contamination. The BE of this peak is between 284.6 - 285.0 eV [2]. XPS is also capable of conducting a depth profile analysis by utilizing Ar ions to mill into the sample. This technique allows for the characterization of thin films as a function of depth and was utilized in this study to understand and elucidate the location of SEI within thin films of polymer binders. Here both PVDF and CMC were investigated.

PVDF has been shown to swell with electrolyte, while CMC does not[11]. Comparing the two binders will help to verify if the location of SEI within the binder is dependent on the binder's ability to absorb electrolyte. Thin films of the binders will be spun onto crystal Si wafers. No conductive additives will be utilized such that any results can be directly linked to the presence of the binder.

2.2 Experimental Methods

2.2.1 Thin Film Preperation

Double side polished (111) Si wafers (50.8 mm diameter, 0.5 mm thickness, N-type doped with As, and R: 0.005-0.05 ohm.cm) were purchased from MTI Corporation. The wafers were then sonicated in acetone for 10 mins followed by another 10 min sonication in isopropyl alcohol (IPA).

PVDF (534,000 Mw) was purchased from Sigma-Aldrich and mixed with 1-methyl-2-pyrrolidinone (NMP) from Sigma-Aldrich to make a 6 wt % solution of PVDF in NMP. The solution was mixed at 70 °C at 700 RPMs for 24 hours. The PVDF solution was then spun coat onto a cleaned Si wafer at 500 RPMs for 10 to distribute the binder solution then 5000 RPMs for 30 s to achieve the desired thickness. The wafer was cured on a hot plate for 1 hr at 70 °C.

CMC (250,000 Mw) was purchased from Sigma-Aldrich. Unlike PVDF, CMC is not soluble in NMP and thus a different solvent was needed. Deionized water was first used as the solvent, but adhesion issues between the aqueous solution and the Si wafer hindered the creation of a continuous CMC film on Si. Ding et al. and Mazouzi et al. both showed changing the pH of the aqueous solvent used would help to improve adhesion of CMC to Si[17]. This is due to the promotion of covalent bonding between Si and CMC. Glacial acetic acid was then purchased from Sigma-Aldrich, which was diluted to make a pH 3 solution in deionized water. The pH3 solution was made by diluting the glacial acetic acid into a 0.1 M solution of acetic acid in deionized water. The acetic acid solution was then mixed with the CMC powder to make a 4.5 wt% solution of CMC in acetic acid. The CMC solution was mixed at 70 °C for 24 hrs at 700 RPMs. The CMC solution was then spun coat onto a cleaned Si wafer at 7000 RPMs for 30 s and cured on a hot plate at 70 °C for 1 hr. The wafers with the cured thin films were then diced into 0.5 x 0.5 cm squares, which were used as the working electrode in a coin cell.

To check that the thin films fully coated the Si wafers, scanning electron microscopy (SEM) was conducted. Following the SEM analysis, atomic force microscopy (AFM) was conducted to measure the film thickness. To measure the thickness of the films a razor blade was used to make a cut in the prepared films. The blade was gently run over the sample to prevent piling of the film around the cut.

2.2.2 Coin Cell Fabrication and Electrochemical Testing

Two types of electrochemical tests were conducted: cyclic voltammetry (CV) and galvanostatic test. The cyclic voltammetry (CV) is conducted by sweeping the voltage of a cell at a fixed rate between two potentials and the current response is recorded. This test can help to identify the position of the oxidation and reduction reactions that occur relative to the reference electrode (lithium metal). The voltage sweeping process

is then repeated over multiple cycles to see if any new reactions occur. This test also helps to determine the reversibility of the reactions. For a completely reversible reaction the observed current magnitude during lithiation should be equal to the current magnitude during delithiation.

The galvanostatic testing is done by applying a constant current for a given amount of time with maximum and minimum voltages limits. In this study galvanostatic cycling is done to determine the cycling efficiencies of binder coated Si by comparing the total charge observed after lithiation to the total charge after delithiation as shown in equation 2.2

$$Efficeincy = \frac{Q_{delith}}{Q_{lith}} * 100 \tag{2.2}$$

Where Q_{delith} is the total charge after delithiation and Q_{lith} is the total after lithiation. Any discrepancies in cycle efficiencies can be linked to the presence of the binder.

2032 coin cells were assembled by first sonicating the coin cell hardware (coin cell cases, 100 μm spacer, and wave spring) in IPA for 10 minutes. A digital photograph was taken of the Si chips prior to cycling. This was done to measure the surface area of the diced chips using ImageJ software. Si electrode surface area was used to normalize current density and observed capacity for each sample.

The hardware, working electrode (bare Si or binder coated Si), and polymer separator (Celgard 2325) were then vacuum heated at 70°C for 24 hrs to remove any residual moisture. The coin cells were then assembled in an argon filled glovebox. The coin cells consisted of a 500μm thick lithium foil counter electrode, 100 μL of electrolyte, Celgard separator, working electrode, a single steel spacer, and a single steel wave spring as seen in Figure 2.1. The coin cells were crimped at 750 psi

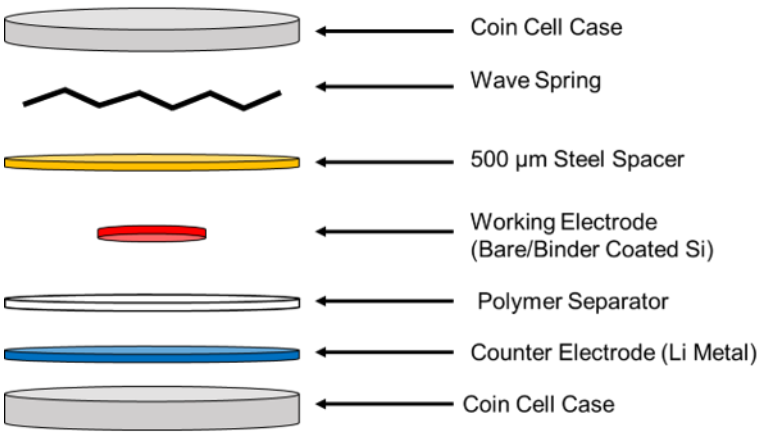

Figure 2.1 Schematic of a single 2032 coin cell. This schematic highlights the individual components of the cell as well as the order in which they are placed relative to each other.

with a hydraulic crimper (MTI Corp) and then removed from the glovebox. The coin cells' voltage was then measured with a voltmeter to ensure that no short circuiting occurred.

Electrochemical cycling was then performed on the fabricated coin cells. A cyclic voltammogram (CV) study was conducted by cycling the cells between 0.01 V and 2 V vs. Li/Li+ at a scan rate of 0.1 mV/s. Any peak density that was observed was attributed to a chemical reaction that occurred within the cell. Peak current density values as well as peak locations were compared to see how the presence of the two binders affected the lithiation and delithiation of Si. The cells were cycled 5.5 times and terminated in their lithiated state.

A galvanostatic study was then conducted by applying a constant current density of 25 μA/cm2. The voltage cutoffs for the test were 0.05 V vs. Li/Li+ for lithiation and 1.2 V vs. Li/Li+ for delithiation. Each step also had a time cutoff of 25 hrs implemented. A time cut off was implemented such that the first lithiation will occur and a set volume of Si will react with lithium and change its phase to an amorphous lithiated Si. The cell will then fully delithiate and after subsequent cycling, the time cut off will prevent more Si from alloying with lithium thus allowing

for a set volume of active material to cycle. The cells were cycled 10 times and their areal capacity was calculated for each lithiation/delithiation cycle.

2.2.3 XPS Analysis

After CV testing the coin cells were disassembled in an Ar filled glovebox with moisture and oxygen content below 5 ppm. The electrodes were rinsed with dimethylcarbonate (DMC) twice to remove any unwanted residual electrolyte. The electrodes were then mounted into an inert transfer vessel using double sided-tape, which helped to electronically isolate the samples. The samples were then inserted into a Versaprobe II scanning X-ray photoelectron spectrometer Microprobe from Physical Electronics USA, Inc. The Versaprobe II utilizes a monochromatic Al Kα X-ray source which enhances lateral resolution to enable precise analysis of a desired region of the sample. A duel neutralizing approach utilizing low-energy electrons and low-energy Ar ions was applied.

A survey was first conducted to identify the elemental regions present in the cycled films. Following the survey, multiplex measurements were taken in the C1s, O1s, F1s, Li1s, Na1s, P2p, and Si2p photoelectron regions. The X-ray beam was electronically rastered over the analyzed region to minimize the damage due to X-ray exposure. The analyzer pass energy for the survey scans was set to 117.4 eV, while the analyzer pass energy was set to 23.5 eV for the multiplex spectra. This resulted in an analyzer resolution of 1.76 eV for the survey spectra and 0.35 eV for the multiplex spectra. In the case of the pristine films, the BE was calibrated such that the lowest BE peak in the C1s region corresponded to 284.8 eV of adventitious carbon contamination. In the case of the cycled films the BE was calibrated such that 685.0 eV represent LiF in the F1s region.

After the survey and multiplex were finalized, 30 mins of depth profiling was conducted utilizing C-60 fullerene ions. The C-60 ions were utilized opposed to the

standard Ar-ion milling because Ar-ion milling has been found to alter the chemical state of certain compounds after long exposure. One specific compound is PVDF, thus making it imperative to use the C-60 milling. The chemical degradation of PVDF due to Ar-ion sputtering can be found in Appendix A (Figures A.1 and A.2).

During the 30 mins of sputtering, multiplex studies were conducted at 5 min, 10 min, 15 min, and 30 min. This was done such that high resolution scans could be taken at different depths in the sample. By characterizing the compounds found at different depths, it became possible to understand not only the location of SEI compounds within the binder, but also the change in the atomic percentage of these compounds as a function of depth.

The compositing and deconvolution of the elemental regions was performed using XPSPEAK 4.1 software. The background was fit using a Shirley type background function, while a mixed (80/20) Gaussian-Lorentzian peak was utilized. The peak fitting process involved optimizing the peak parameters of a well resolved region. The peak parameters include the full width half-maximum (FWHM), the peak position, and the area. Once well resolved peaks were optimized, additional peaks were added in order to minimize the chi-squared value. Doublet peaks were utilized when deconvoluting the Si2p and P2p regions. The doublet peaks were constrained such that they optimized together. Each photoelectron region was then compared to ensure that the atomic percentage of like compounds were in accordance with each other over their shared photoelectron regions (i.e., the atomic percentage of LiF in the F1s region was similar to the atomic percentage of LiF in the L1s region).

2.3 Results and Discussion

Figure 2.2 shows the SEM images of both CMC (A) and PVDF (B) films, and it can be noted that they uniformly coated the surface of the Si wafer. It is important to note that the PVDF film shows an interesting pattern resembling grain structure in

metals. Never the less the film is continuous, and the roughness is negligible relative to the thickness. The PVDF film was measured to be 282.25 nm, while the CMC film was measured to be 310 nm.

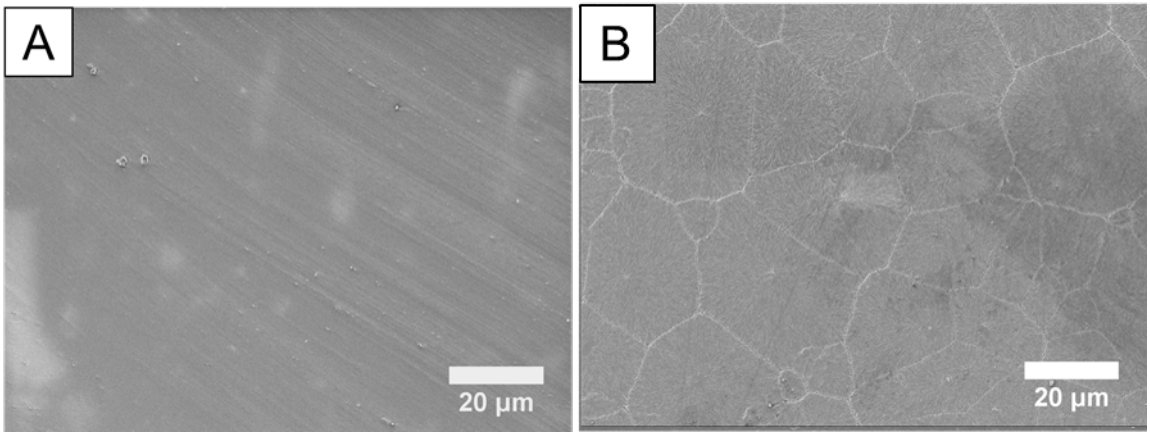

Figure 2.2 Scanning Electron Microscopy (SEM) micrographs of CMC (A) and PVDF (B) on Si.

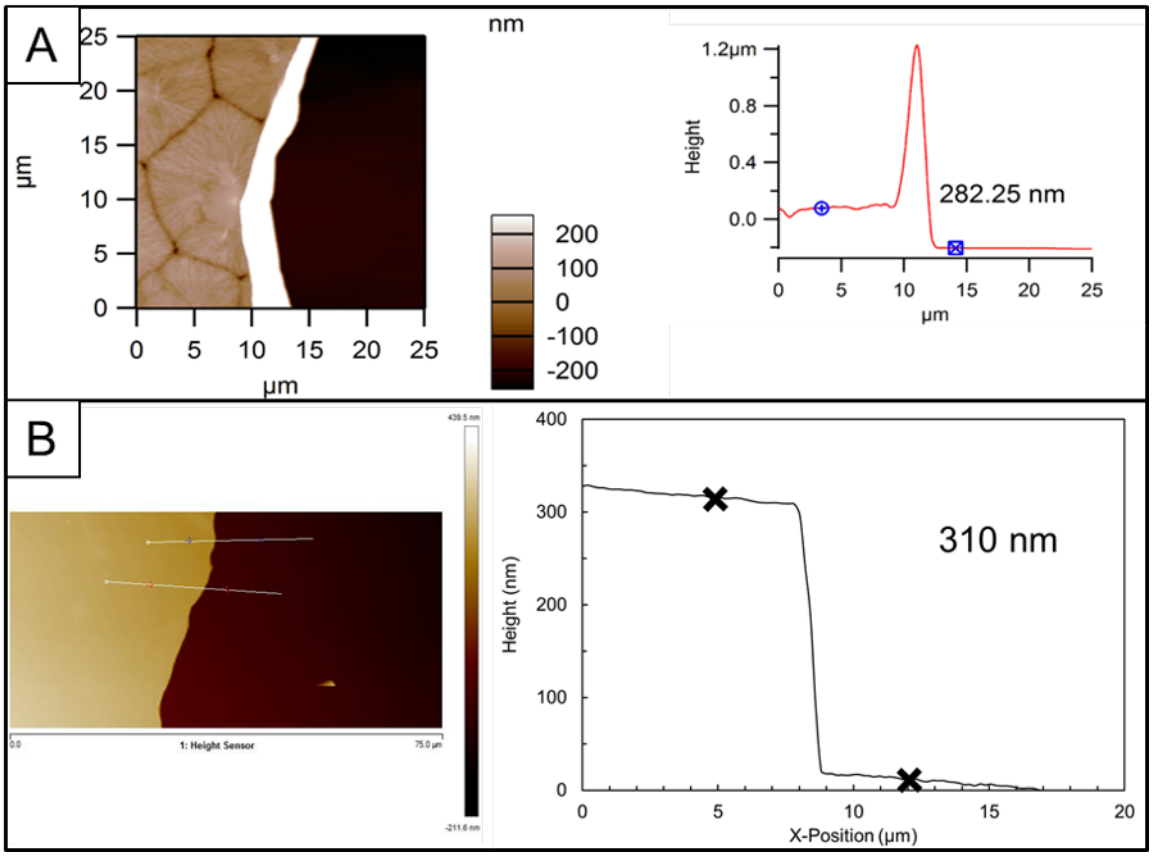

Figure 2.3 Atomic force microscopy (AFM) images of PVDF (A) and CMC (B) with corresponding thickness measurements. The PVDF film was found to be 282.25 nm, while the CMC film was found to be 310 nm.

2.3.1 Electrochemical Performance

To understand the effect of binder on the cycling behavior of Si, CV studies were performed. By performing these tests, the reactions that occur during cycling can be observed in which a peak will form at a specific potential that represent a phase change or chemical reaction. By comparing the bare Si sample to the binder coated samples, any differences in electrochemical performance can be attributed to the presence of the binder since all samples will be cycled similarly. Furthermore, if the magnitude of the peak current density is different between the coated and bare samples, it can be concluded that the binder will affect the kinetics of lithiation.

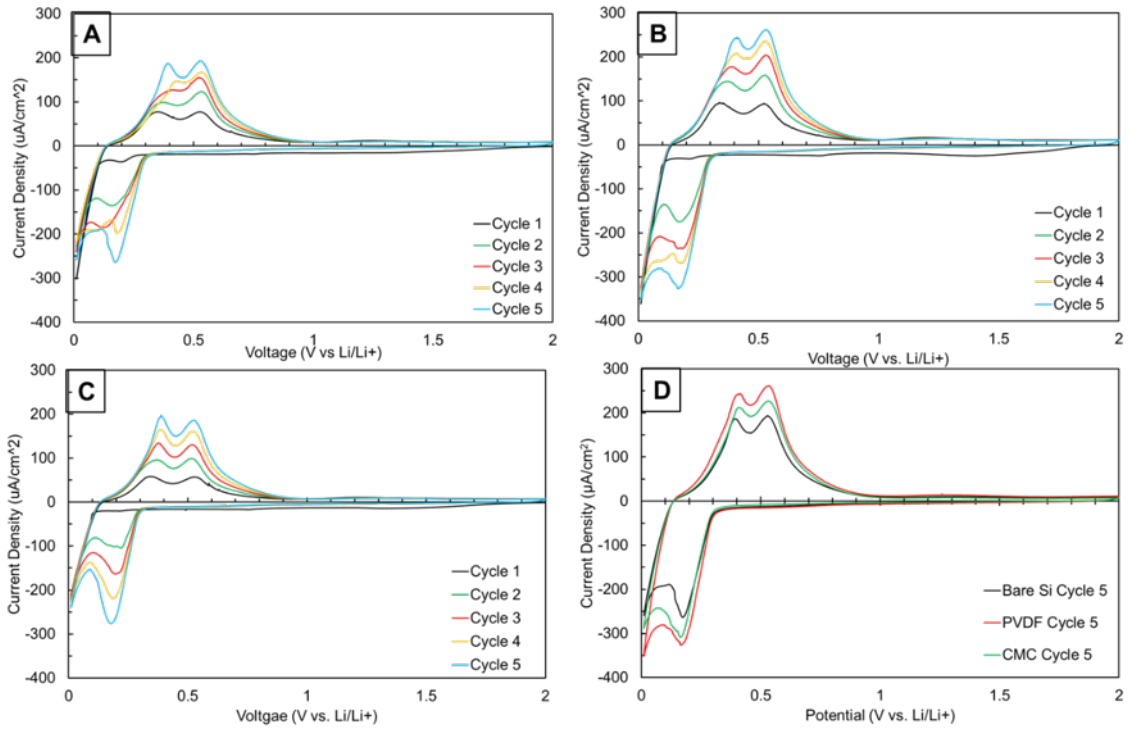

Figure 2.4 Cyclic voltammetry response of bare Si (A), PVDF coated Si (B), and CMC coated Si (C) after five cycles. The fifth cycle of each of the samples were overlaid (D) to show their agreement.

Figure 2.4 shows the CV response of bare Si (A), PVDF coated Si (B), and CMC coated Si (C). A comparison of the responses of these three samples was then made in Figure 2.4 D in which the fifth cycle of each sample is overlaid. At 0.1 V vs. Li/Li+ a sharp decrease in current was observed which was synonymous with the onset of lithium alloying with Si[27]. As the cells delithiate two oxidation (or anodic) peaks are observed at 0.35 V vs. Li/Li+ and 0.55 V vs. Li/Li+ which represent the dealloying of lithium[24]. As the cells began their second lithiation a new peak was observed at 0.2 V vs. Li/Li+ which represent the lithium alloying with Si [24]. With each new cycle the peak current densityincreased in magnitude for all observed peaks, which can be attributed to the electrochemical activation of additional crystalline Si in each cycle. As the wafer cycles, cracks are formed on the surface which exposed

more Si to subsequently react with lithium[24], thus increasing the observed peak current density.

When comparing the CV response of the binder coated samples to the bare Si sample, there is little to no difference observed in peak position. This comparison can be seen in Figure 2.4 D where the fifth cycle of the PVDF coated Si, CMC coated Si, and bare Si CVs were plotted. Each sample shows a peak reduction current density of roughly -370 μA/cm2 and a peak oxidation current density of roughly 250 μA/cm2. The comparable peak positions after 5 CV cycles helped to show that the presence of binder did not affect the electrochemistry since no new observed peaks were found when the binder was present.

To further verify that the PVDF and CMC had no effect on the electrochemical performance of the Si, galvanostatic tests were conducted and the efficiency of the cells were calculated and compared. This was done by first calculating areal capacity of the cells and then plotting against the observed potential. The voltage plot of cycled bare Si, PVDF coated Si, and CMC coated Si can be seen in Figure 2.5 After five cycles their efficiencies were calculated and tabulated in Table 2.1. Overall, the three samples show good agreement in both behavior and cycle efficiency[5]. The observed first cycle efficiency of the PVDF coated sample was 65%, the first cycle efficiency for the CMC coated sample was 69%, and the first cycle efficiency of the bare Si sample was 71%. After five galvanostatic cycles, each sample reached 99% efficiency.

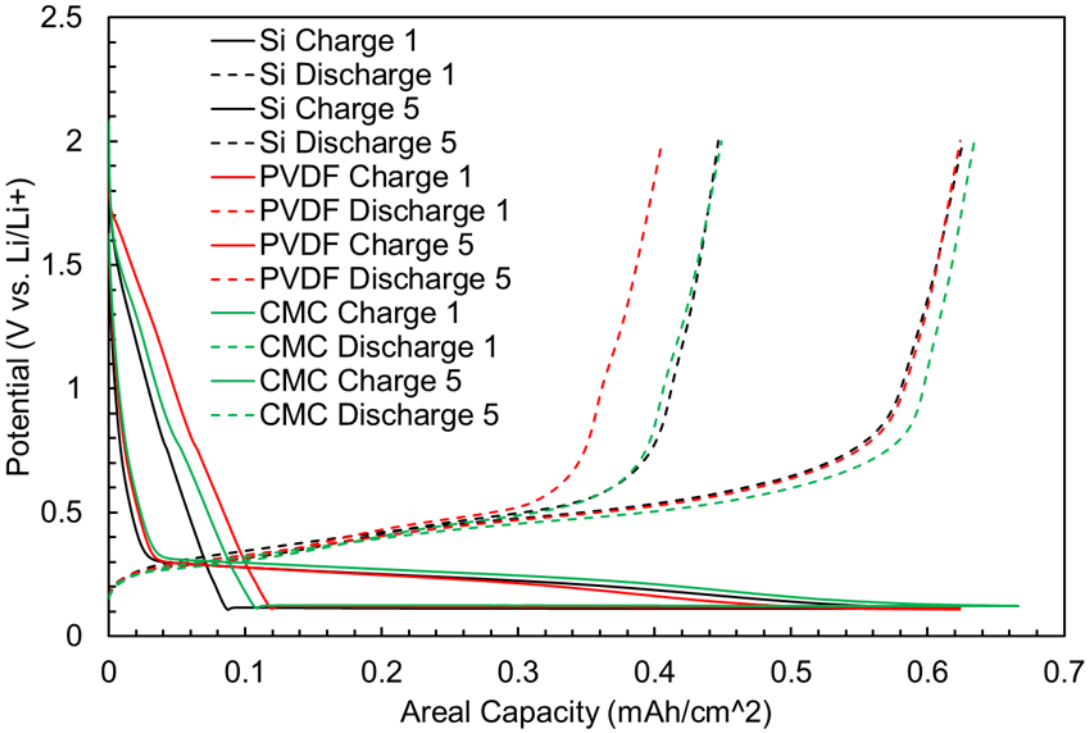

Figure 2.5 Voltage curves of bare Si (black), PVDF coated Si (red), and CMC coated Si (green) after their first and fifth cycle of galvanostatic testing. Each charge cycle is represented by a solid line and each discharge cycle is represented by a dotted line.

These results helped to verify the observed cycling behavior seen from the CV testing because the first cycle efficiency of all three samples were comparable. Furthermore, as the sample underwent further cycling the efficiency were also comparable implying that the binder did not influence the overall cycling performance.

Table 2.1 Cycle Efficiency of Bare Si, PVDF Coated Si, and CMC Coated Si

Cycle	Bare Si Efficiency	PVDF Efficiency	CMC Efficiency
1	71	65	69
2	81	82	84
3	93	93	94
4	98	98	98
5	98	99	98

2.3.2 Effect of Binder on SEI Formation

XPS analysis was first conducted on bare Si and uncycled films to obtain a benchmark which then can be compared to all the cycled data. Figures 2.6 and 2.7 show the deconvoluted C1s spectra of uncycled PVDF and uncycled CMC respectively. The two large peaks at 285.9 eV and 290.4 eV shown in Figure 2.6 in the C1s region associated with C-C and C-F bonding are representative of the PVDF film. In the F1s region a single peak at 687.6 eV was observed, which was also representative of the PVDF film. The peak parameters of the uncycled PVDF film are shown in Table 2.2. The atomic percentage of the two PVDF associated peaks in the C1s region and the single peak in the F1s combined to make up ∼98% of the surface chemistry implying the film was not chemically altered due to the sample preparation.

When analyzing the uncycled CMC film two peaks associated with the CMC were seen in the C1s region located at 286.3 eV and 288.0 eV[23]. The third peak in the C1s region is representative of hydrocarbons. When analyzing the O1s region there were three peaks as well. One located at 531.1 eV representing the C-O bonding in the CMC, one located at 532.7 eV representing the other oxygen containing compounds of the CMC, and a final peak at 535.7 eV representing the Na Auger[23]. The Na Auger is an artifact of the sodium that is in the film. Although the Auger appears in the O1s

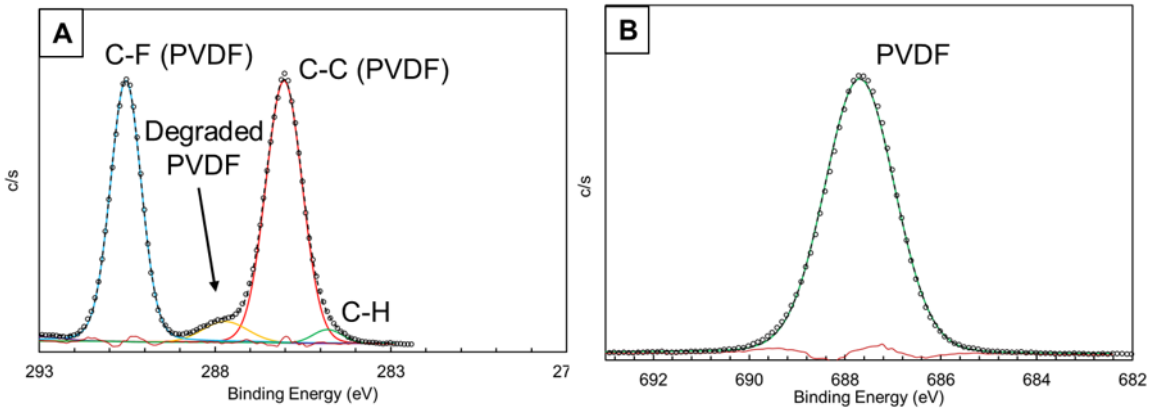

Figure 2.6 Deconvoluted C1s region (A) and F1s region(B) of uncycled PVDF on Si.

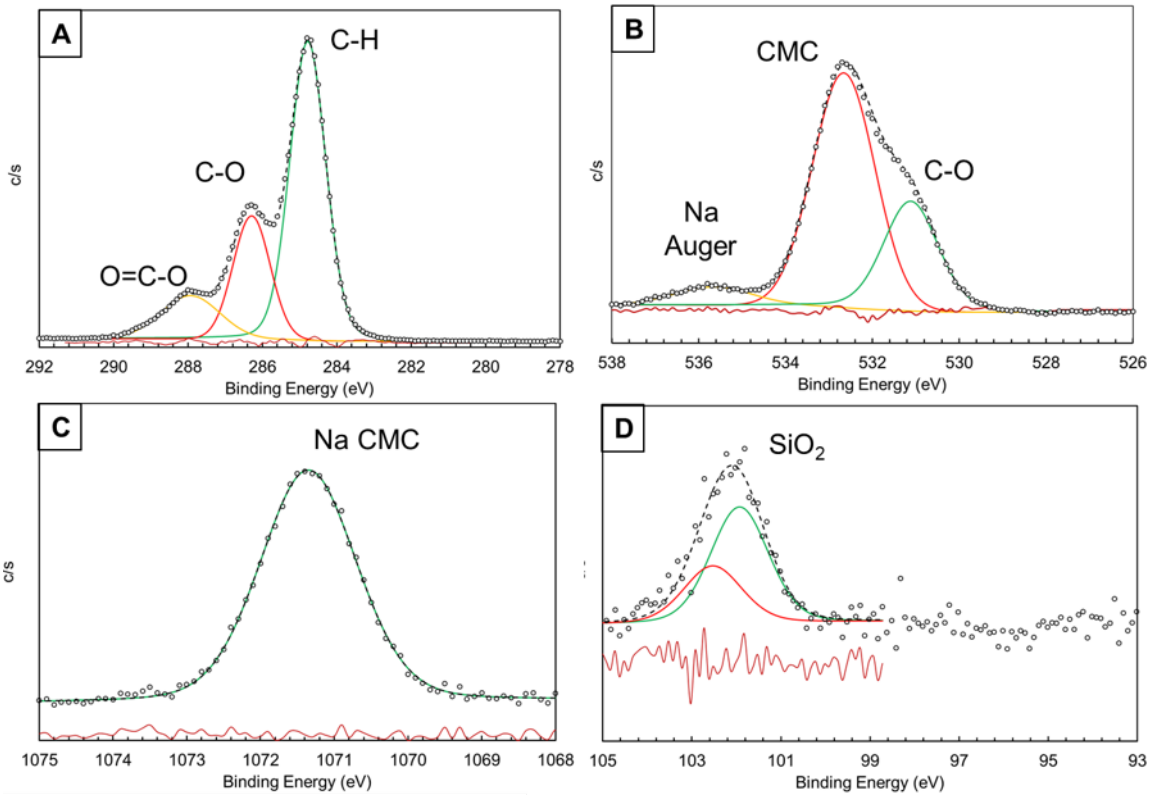

Figure 2.7 Deconvoluted C1s (A), O1s (B), Na1s (C), and Si2p (D) regions of uncycled CMC on Si.

region it is not an oxygen containing compound. A single peak was then observed in the Na1s region which represented the sodium found the CMC film. Finally, a low atomic percentage SiO_2 peak was observed at 102.1 eV. The presence of this peak was due to Si contamination that was present due to dicing of the electrodes which was based on the low atomic percentage observed.

Table 2.2 XPS Summary of Uncycled PVDF on Si. This Table Shows the Binding Energy, FWHM, Atomic Percentage, and Assignment of all Deconvoluted Peaks. The Shake Up Seen in the C1s Region Represents an Artifact of XPS Analysis

C1s				
Peak	BE	FWHM	Atomic %	Assignment
1	284.8	1.2	1.5	C-H
2	285.9	1.2	24.6	C-C
3	287.6	1.7	2.6	Degraded PVDF
4	290.4	1.1	21.5	C-F
5	292.7	1.5	0.6	Shake Up
F1s				
Peak	BE	FWHM	Atomic %	Assignment
1	687.6	1.7	49.1	C-F

Once the uncycled films were properly understood and characterized, the cycled bare Si samples were analyzed. The bare Si samples were used to fully understand the expected signature of the SEI formed during electrochemical cycling. C-60 depth profiling was also conducted on these samples to fully understand the distribution of SEI compounds as a function of depth.

The result of the XPS deconvolution of the surface of the bare Si samples can be seen in Figure 2.8. The surface of the cycled Si is predominately comprised of hydrocarbons, LiF, Li_2CO_3, and reduced electrolyte. The atomic percentages as well

Table 2.3 Summary of Uncycled CMC on Si. This Table Shows the Binding Energy, FWHM, Atomic Percentage, and Assignments of all Deconvoluted Peaks

C1s				
Peak	BE	FWHM	Atomic %	Assignment
1	284.8	1.1	43.5	C-H
2	286.3	1.2	17.4	C-O
3	288	1.9	9.8	O=C-O
O1s				
Peak	BE	FWHM	Atomic %	Assignment
1	531.1	1.5	7.4	C-O
2	532.7	1.7	16.2	CMC
3	535.7	2.1	1.6	Na Auger
Na1s				
Peak	BE	FWHM	Atomic %	Assignment
1	1071	1.5	3.5	CMC
Si2p				
Peak	BE	FWHM	Atomic %	Assignment
1	102.1	1.5	0.6	SiO_2

as the peak location of these compounds can be seen in Table 2.4. The observed compounds are synonymous with SEI and helped to verify that a stable SEI layer was formed on the surface of the cycled electrodes while also providing valuable information regarding the SEI composition that should be present in the binder coated films[21]. C-60 sputtering was then conducted on the sample to further understand the composition of SEI, specifically at the interface of SEI and Si.

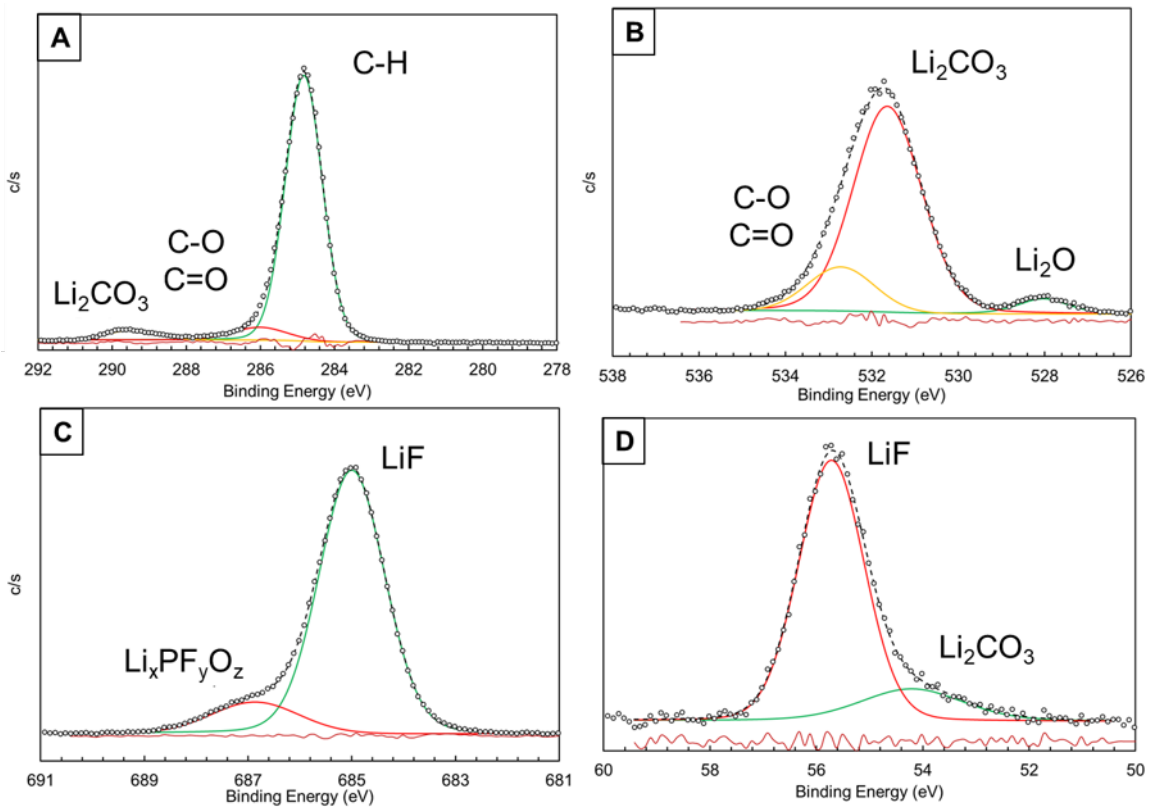

Figure 2.8 Deconvoluted C1s (A), O1s (B), F1s (C), and Li1s (D) regions of the surface of bare Si after 5.5 cycles of CV tests.

Figure 2.9 shows the deconvoluted C1s (A), O1s (B), F1s (C), and Li1s (D) regions of the cycled bare Si sample after C-60 sputtering. Table 2.5 shows the summary of the peak parameters. From the C-60 sputtering, it was observed that the atomic percentage of Li_2O increased while the atomic percentage of Li_2CO_3 and LiF were reduced. These observations were compared to the literature which states that the composition of the SEI formed on Si should be dominated by Li_2O at the interface of SEI and Si. Thus, the results of the C-60 sputtering corresponded to the expected results from the literature[21] [23].

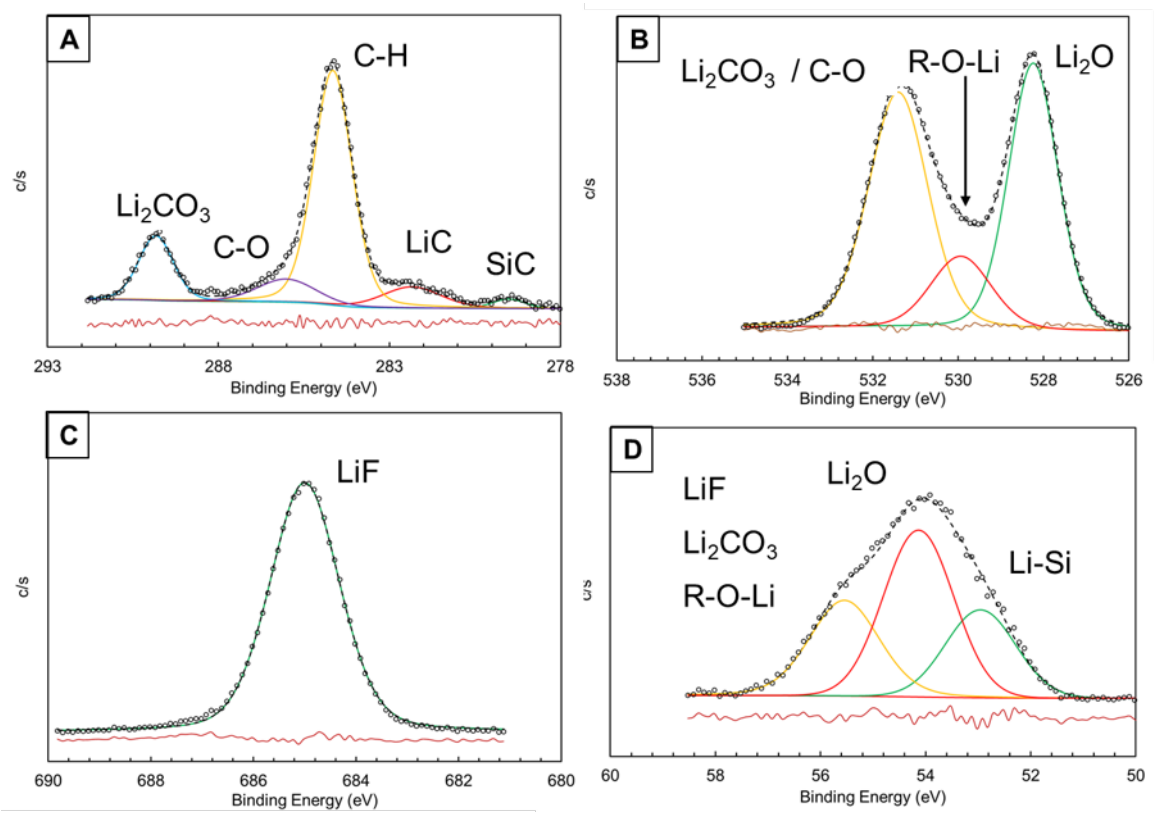

Figure 2.9 Deconvoluted C1s (A), O1s (B), F1s (C), and Li1s (D) regions of the bare cycled Si after C-60 sputtering.

With the composition of the SEI formed on bare Si characterized at both the surface and the interface, the binder coated samples were then analyzed. XPS analysis was conducted at the surface, within the binder, and at the interface between binder and Si. The depth profiling was conducted by sputtering the samples for 30 mins using C-60 ion milling. The samples were then analyzed after 5, 10, 15, and 30 mins. At each interval a high resolution scan was conducted to analyze the chemical composition after sputtering. The relative location of the XPS analysis conducted at each interval was found by first plotting the atomic percentage of both the C1s and Si2p regions of the binders as a function of C-60 sputter time. As the sputter time increased the atomic percentage of the C1s region decreased while the atomic percentage of the Si2p region increased. The crossover point of these two elemental regions represents the breakthrough point, or the interface between binder and Si.

Table 2.4 XPS Summary of Bare Si After 5.5 Cycles of CV Testing. This Table Shows the Binding Energy, FWHM, Atomic Percentage, and Assignments of all Deconvoluted Peaks

C1s				
Peak	BE	FWHM	Atomic %	Assignment
1	285	1.2	34	C-H
2	286	1.7	2.6	C=O/C-O
3	290	1.6	1.7	Li_2CO_3
O1s				
Peak	BE	FWHM	Atomic %	Assignment
1	528	1.3	0.4	Li_2O
2	532	2	6.6	Li_2CO_3
3	533	1.8	1.3	C=O/C-O
F1s				
Peak	BE	FWHM	Atomic %	Assignment
1	685	1.5	19.8	LiF
2	687	2	2.9	$Li_xPF_yO_z$
Li1s				
Peak	BE	FWHM	Atomic %	Assignment
1	54.2	2.3	4.8	Li_2CO_3
2	55.7	1.5	23.6	LiF
P2p				
Peak	BE	FWHM	Atomic %	Assignment
1	134	2.2	0.2	$Li_xPF_yO_z$
2	137	1.7	0.3	Li_xPF_y
Si2p				
Peak	BE	FWHM	Atomic %	Assignment
	102	1.8	0.8	SiOx

The time was then recorded and used to calculate the sputter rate. This was done by diving the binder's thickness by the breakthrough time. The breakthrough of both PVDF and CMC can be seen in Figure 2.10.

Table 2.5 XPS Summary of Bare Si After C-60 Sputtering. This Table Shows the Binding Energy, FWHM, Atomic Percentage, and Assignments of all Deconvoluted Peaks

C1s				
Peak	BE	FWHM	Atomic %	Assignment
1	279.51	1.13	0.3	SiC
2	282.34	2	1	LiC
3	284.65	1.33	7.5	C-H
4	286.02	2	1.1	C-O
5	289.83	1.2	1.9	Li_2CO_3
O1s				
Peak	BE	FWHM	Atomic %	Assignment
1	528.24	1.36	11.9	Li_2O
2	529.94	1.68	4	R-O-Li
3	531.4	1.64	12.6	Li_2CO_3/C-O
F1s				
Peak	BE	FWHM	Atomic %	Assignment
1	685	1.6	9.4	LiF
Li1s				
Peak	BE	FWHM	Atomic %	Assignment
1	52.95	1.57	11.4	Li-Si
2	54.13	1.57	21.7	Li_2O
3	55.54	1.57	13.6	LiF/Li_2CO_3/R-O-Li
Si2p				
Peak	BE	FWHM	Atomic %	Assignment
1	95.95	1.37	2.4	Li-Si 2p3/2
2	96.55	1.37		Li-Si 2p1/2
3	97.72	1.72	0.4	Si 2p3/2
4	98.32	1.72		Si 2p1/2
5	100.28	1.72	0.7	SiC 2p3/2
6	100.88	1.72		SiC 2p1/2

With the sputter rate calculated, the relative depth at which high resolution scans were taken during C-60 sputtering were calculated and it was found that the scans taken after 5 mins were 150 nm into the film. The breakthrough of the samples occurred after 11 min of sputtering and thus the scan taken after 10 mins of sputtering was used to quantify the chemical composition at the interface of binder and Si. The results of the XPS analysis conducted on the surface, within, and at the interface between PVDF and Si are shown in Figure 2.11. The peak parameters of the PVDF coated sample at all three regions can be found in Appendix B.

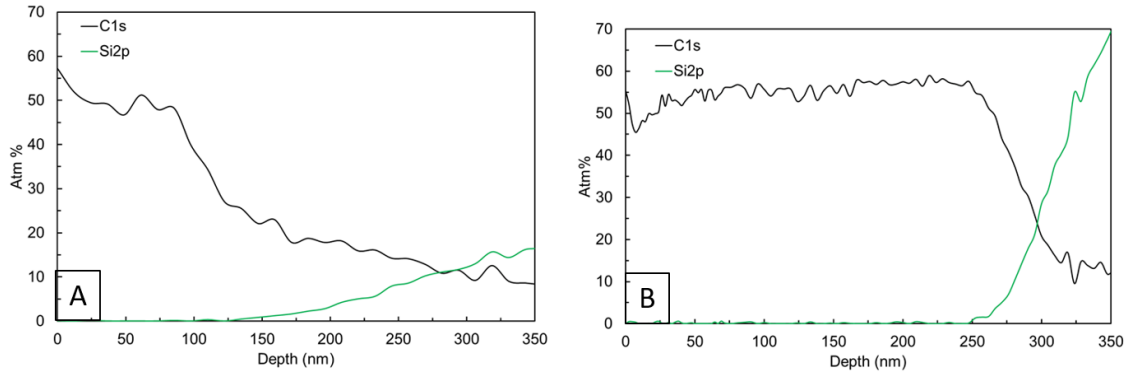

Figure 2.10 Breakthrough of PVDF (A) and CMC (B). The crossover point of the two curves represents the point at which the binder was milled away to expose the underlying Si.

On the surface of the PVDF there were two major peaks in the C1s region which represent the C-C and C-F bonding of PVDF. Unlike the bare Si sample there is no Li_2CO_3 present on the top surface of the binder, however there is an increase in the C-H peak as well as a new peak at 287.4 eV that represents C=O bonding. The increase in atomic percentage of C-H bonding after cycling was ~6%. In the O1s region there was a single peak which is representative of the C=O bonding, and in the Si2p region there was a peak at 102.3 eV representative of SiO_2.

These findings were unexpected because the XPS analysis showed that there was little to no characteristic SEI compounds on the surface of the PVDF. The C=O

peak in the O1s region and the increase is C-H in the C1s region can be linked to the formation of organic SEI components, but they only represent ∼8% of the surface chemistry. Li_2CO_3 and LiF were not present on the surface of the cycled PVDF despite having a strong signal on the surface of cycled Si. This implies that SEI did not form on the surface of the PVDF.

When analyzing the XPS results taken within the PVDF a peak at 289.7 eV repressing Li_2CO_3 was observed in the C1s region as well as peaks repressing C-C, C-F, C=O, and C-H bonding. In the O1s region there were peaks observed at 528.4 eV and 531.2 eV. These two peaks represented Li_2O and Li_2CO_3 respectively. Like the surface of the PVDF, there was also a peak at 532.8 eV representing C=O bonding. The Si2p region showed two peaks, one at 96.3 eV and one at 101.1 eV. These two peaks represented Li-Si and Si, though their atomic percentage was ∼0.1%. It is important to also note that the atomic percentage of LiF within the binder was 35% which is comparable to the 40% found in the top surface of the cycled Si. Unlike the surface of the PVDF, the results of the XPS analysis conducted within the binder showed that SEI was formed and that the composition was similar to the composition of the SEI found on the top surface of the bare Si.

Finally, XPS analysis was conducted at the binder/PVDF interface. In the C1s region there were peaks representing SiC, LiC, C-H, C-C, C=O, C-F, and Li_2CO_3. The presence of SiC was due to the C-60 sputtering process in which carbon was embedded into the Si with an increase in sputter time. Like the cycled bare Si, the Li_2CO_3 peak was reduced at the PVDF / Si interface. When analyzing the O1s region a strong Li_2O peak was observed at 528.3 eV. When comparing the atomic percentage of Li_2O at the PVDF / Si interface to the atomic percentage of Li_2O at the Si / SEI interface of the bare Si sample it was found that the PVDF sample was 23% while the Si sample was 33%. Again, these two values are comparable and help to show that

the SEI formed in the PVDF was similar to the SEI formed at the SEI / Si interface of the cycled bare Si sample.

With all three regions of the PVDF sample analyzed it was clear that SEI formed predominately in the binder, while little to no SEI formed on the top surface. The region analyzed that was roughly in the center of the PVDF film showed an SEI composition that was comparable the SEI formed on the top surface of the bare Si sample. The composition of the SEI at the PVDF / Si interface was similar to the SEI / Si interface of the bare Si sample which was conclude based on both samples being dominated by Li_2O. The location of the SEI within the binder is in accordance with the fact that PVDF swelled with electrolyte. Since the electrolyte was present within the PVDF, SEI compounds were formed with it. This result is of vital importance because it shows that SEI was present within the binder, which could affect the adhesion of PVDF to Si and thus explain its poor performance when compared to CMC and other binders.

CMC was then analyzed to understand the location of the SEI formed within it. The deconvoluted peaks of the CMC at the surface, within the binder, and at the CMC / Si interface is shown in Figure 2.12. The peak parameters of the CMC can be found in Appendix B.

On the top surface of the cycled CMC sample there were three peaks in the C1s region representing C-H, C-O, and O=C-O bonding. When compared to the uncycled CMC sample there were little to no discrepancies in the C1s region and no Li2CO3 was observed. The O1s region of the cycled sample again showed little to no deviation from the uncycled CMC film. However, two major SEI compounds were observed in the F1s region which were LiF and $Li_xPF_yO_z$. The LiF made up 5% of the chemical composition, while the reduced electrolyte made up 11% of the chemical composition. Unlike the PVDF sample, the CMC sample had SEI compounds observed on the top surface, but it was not comparable to the SEI seen in the bare Si sample. This is

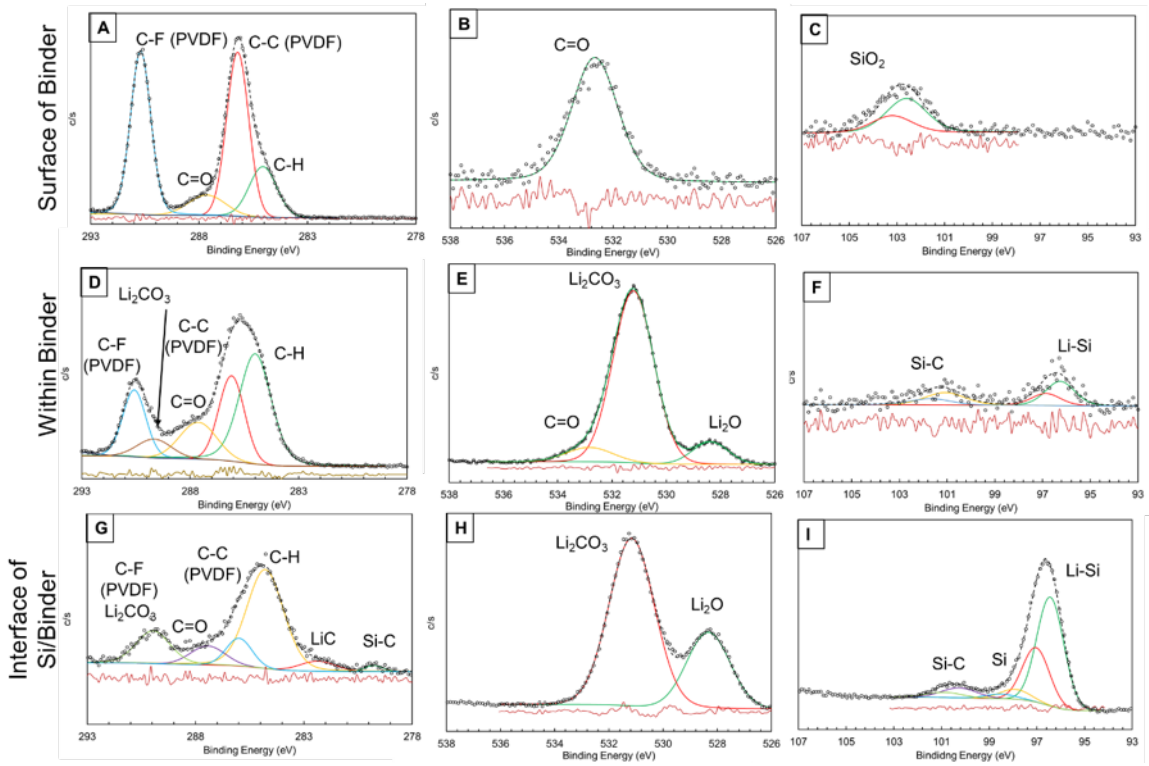

Figure 2.11 Deconvoluted XPS spectra of PVDF on the surface of the binder, within the binder, and at the binder / Si interface. The C1s, O1s, and Si2p regions of the surface of the binder are shown in (A-C). The C1s, O1s, and Si2p regions within the binder are shown in (D-F). The C1s, O1s, and Si2p regions of the binder / Si interface are shown in (G-I).

because the CMC sample had substantially more reduced electrolyte on its top surface when compared to the bare Si sample, as well as less LiF and no Li2CO3.

The chemical composition of the CMC sample after 5 mins of sputtering was then observed to verify if SEI compounds formed within the it. The C1s region showed the same three peaks as the top surface of the sample, but the intensity of the C-O peak was drastically reduced. The O1s region also showed a reduction of the peak associated with the CMC at 530.5 eV. Interestingly, the F1s region showed a drastic change in which the peak associated with the reduced electrolyte was no longer present, but the LiF signal was the same. What was more interesting was that there was no signal for lithium at all during sputtering. This is interesting because

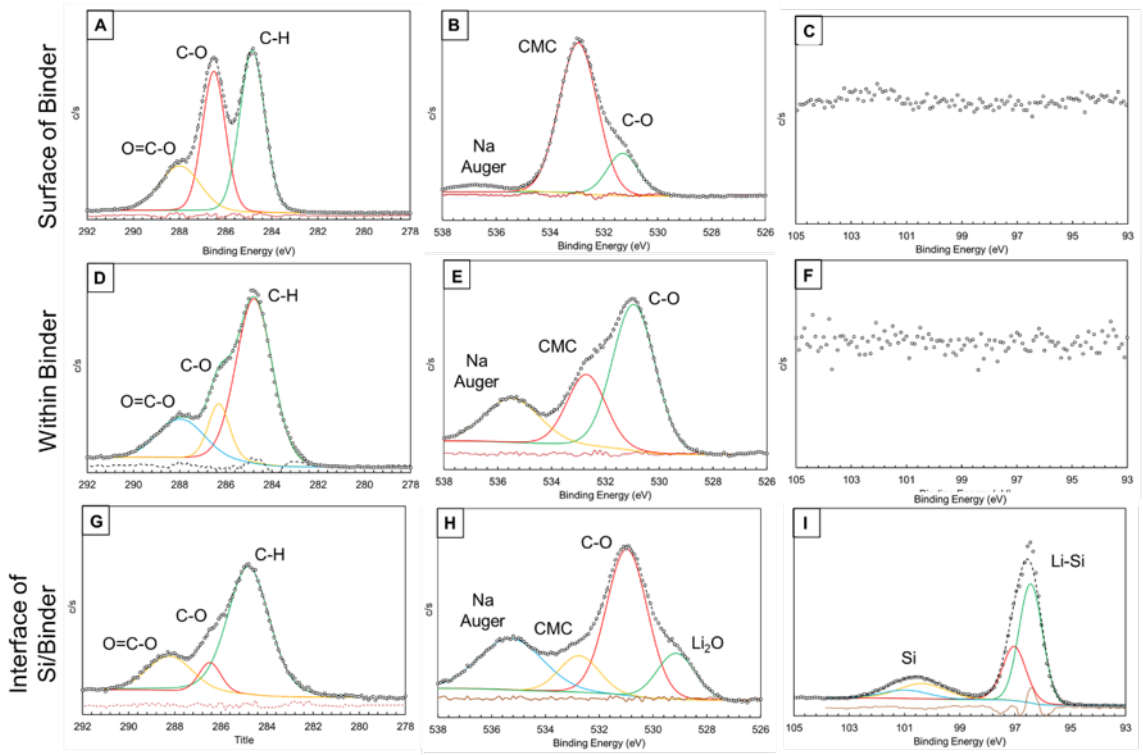

Figure 2.12 Deconvoluted XPS spectra of CMC on the surface of the binder, within the binder, and at the binder / Si interface. The C1s, O1s, and Si2p regions of the surface of the binder are shown in (A-C). The C1s, O1s, and Si2p regions within the binder are shown in (D-F). The C1s, O1s, and Si2p regions of the binder / Si interface are shown in (G-I).

the majority of the characteristic SEI compounds contain lithium, so the lack of a presence of these compounds implies a lack of SEI within the CMC sample.

The interface of CMC and Si was then analyzed. In the O1s region there was a peak associated with Li_2O at 528.4 eV, but its atomic percentage was only 2.5% which was low when compared to the 23% and 33% found in the PVDF and bare Si sample. All other elemental regions showed a similar lack of SEI containing compounds. Despite the lack of SEI there was still Li-Si found at the interface of the CMC sample. The presence of Li-Si proves that the CMC sample was properly lithiated. The presence of Li-Si coupled with the comparable electrochemical response of the CMC sample to both the PVDF and the bare Si sample implies that unlike PVDF, CMC does not allow for the formation of SEI within it. This result helps

to further explain CMC's performance when compared to PVDF when utilized in a composite electrode. Since no SEI is present within the film, the adhesion between CMC and Si would not be altered due to electrochemical cycling and thus CMC would have improved performance.

2.4 Conclusions

Thin films of both PVDF and CMC were spun coat onto crystal Si wafers and electrochemically cycled. The results of the electrochemical cycling showed that the presence of the thin films did not alter the electrochemistry during cycling. The cycled samples were then disassembled and XPS analysis was conducted in connection with C-60 sputtering. The results of the XPS analysis of the top surface of the bare Si showed that a characteristic SEI layer was formed during cycling that was comparable to the literature. The surface chemistry of the PVDF coated sample showed little to no SEI compounds, while the surface of the CMC sample showed a large atomic percentage of reduced electrolyte as well as a small percentage of LiF. C-60 sputtering was then conducted to characterize the SEI found within the binders. The PVDF sample had an SEI composition that was comparable to the SEI found on the top surface of bare Si, while the CMC sample showed no SEI formation. C-60 sputtering was then continued until the binder was milled through and the interface between binder and Si could eb characterized. At the interface of PVDF and Si there was again a characteristic SEI layer observed. At the interface of CMC and Si there was only a small percentage of Li_2O.

These results show that PVDF allowed for the formation of SEI within it, while the CMC prevented SEI formation. This information sheds light onto the improved cyclic performance of composite anodes that incorporate CMC. Since no SEI forms within the CMC the interface properties will not change due to the presence of new SEI compounds. PVDF however allows for the formation of SEI within it and thus

the interface properties are altered as SEI forms in the binder as well as on the Si. The formation of SEI in the PVDF was attributed to the PVDF's ability to swell with electrolyte.

CHAPTER 3

FABRICATION OF AN IDEALIZED COMPOSITE ANODE

3.1 Background Information

Due to its high theoretical capacity, silicon is a highly sought after material to incorporate into the anode of LIBs. Despite the extremely high theoretical capacity of Si, there is one major drawback to the material that has prevented it from being incorporated in commercial cells and that is the large volume expansion that occurs during cycling. As the Si is lithiated, it can expand up to 300% its original volume only to then reduce in size during delithiation. This extreme volume expansion and contraction can generate stresses that can pulverize the Si while also breaking binder bridges that keep Si particles connected to the electronic network of the anode. Figure 1.1 and Figure 1.2 highlight these binder bridges. Removal from the electronic network electrically isolates the Si which leads to poor cyclic life. Due to the vital role of polymer binders in the composite anode's performance, various binders have been extensively investigated.

To properly predict the cyclic life and performance of Si-based anodes, the quantification and understanding of the stresses that occur within the composite film needed to be understood. Real-time stress measurements coupled with electrochemical response can shed light onto the failure mechanisms that lead to binder bridge failure within the anode. One such real time stress measurement technique is an optical curvature measurement known as multi-beam optical sensing (MOS). Sethuraman et al. used MOS technique to measure the stresses developed in a Si thin film due to electrochemical cycling[26]. In this study amorphous Si was deposited onto an elastic substrate, and it was observed that the substrate constrained the in-plane volume expansion of the thin film which caused a compressive stress to generate within

the film during lithiation. After a compressive stress of 1.7 GPa was reached, the film appeared to flow with further lithiation until the compressive stress was recorded to be 1 GPa. When delithiating the sample there was an initial elastic response until 1 GPa of tensile stress was observed. At this point the film began to flow in tension in order to accommodate the reduction in size corresponding to a reduction in lithium concentration. The stress increased until a tensile stress of 1.75 GPa was recorded. This study characterized the stress response of cycled amorphous Si for the first time.

To characterize the stress response of crystal Si, Chon et al. cycled a Si wafer coupled with MOS measurements[5]. A single cycle of lithiation and delithiation was conducted and the stress response of the crystal wafer was recorded. During lithiation they observed that the crystal wafer experienced a linear increase in compressive stress until the end of the lithiation cycle. They also observed a peak compressive stress of 0.5 GPa. This result implied that the biaxial stress in the amorphous Si layer formed during lithiation was constant. During delithiation there is a sharp linear jump in tensile stress due to the sharp change in lithium concentration. The linear region ends after a stress of 0.5 GPa is recorded, which can be implied as the yield stress of the amorphous Si. As more lithium is removed from the Si, the tensile stress continues to increase until 1.5 GPa of stress is observed. At this point a sharp curvature change occurred which represented the cracking of the Si wafer. They then conducted SEM analysis to confirm the cracking. SEM analysis also showed that the thickness of the amorphous layer formed during cycling was ~ 1 μm. Transmission electron microscopy (TEM) was also conducted to show the phase boundary between amorphous and crystalline Si was atomically sharp.

To further understand the failure mechanisms of the polymer binder, Sethuramen et al. experimentally measured the stress of a composite anode using MOS [25]. Composite films comprised of Si particles, conductive additive, and either PDVF or CMC was spun onto Si substrates. During lithiation the composite electrodes

formulated with CMC showed an initial linear increase in compressive stress, followed by a plateau. The plateau was interpreted as being caused by inter-particle sliding. During lithiation of the PVDF based composite film, failure was observed. This was due to the breaking of binder bridges as the particles increased in size during lithiation. These results showed that CMC out performed PVDF, while also characterizing the stress response of a composite film on an elastic substrate. What was not possible was the measurement the stress at the particle level. The stress that was measured was only the averaged stress throughout the film. This was due to the geometric complexities of the Si particles used in the film.

In order to measure the stress between the active material and the polymer binder, an idealized composite electrode geometry is proposed. A regular array of micro sized cylinders of Si can be used to idealize the distribution of Si particles in a composite anode. Polymer binder can then be added to the system to form binder bridges between the pillars. The idealized anode can then be galvanostaticly cycled, while the curvature is measured. This allows for in situ measurements of both stress and electrochemical response. The idealized composite anode was prepared by microfabrication techniques such that the diameter of the pillars was comparable to micro-sized Si particles used in compote anodes. Both PVDF and CMC were then added to the anode to form binder bridges. The idealized anodes were then electrochemically cycled, and the curvature response was measured. Estimation of the stresses in the binder bridges was attempted by developing a finite element model of the sample.

3.2 Experimental Procedures

3.2.1 Photolithography

Photolithography is one of the most common microfabrication techniques which allows for the transfer of a pattern to a desired material. Photolithography involves multiple steps which are highlighted in Figure 3.1. The first step is to develop a desired pattern using computer aided design (CAD) software.

Once the desired pattern is created the design is transferred to a mask. This process involves depositing chrome onto a quartz substrate. The chrome is then removed such that the pattern created with the CAD software remains, while the rest of the chrome is removed. Once the mask is created, photoresist is spin coated onto a desired substrate.

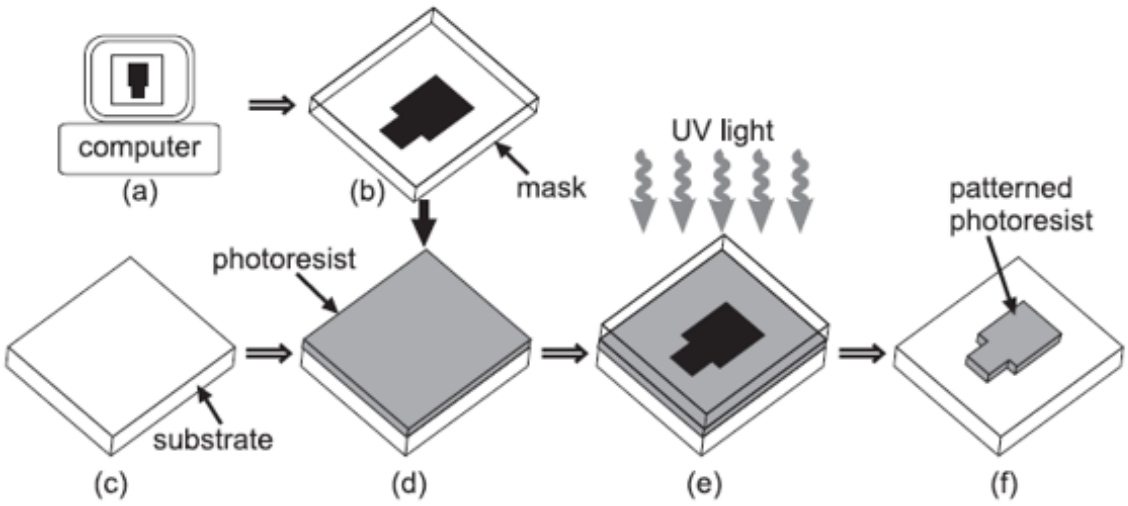

Figure 3.1 Transmission electron microscopy (TEM) image of a thin slice (ca. 300 nm thick) prepared via FIB cross-section of a partially lithiated Si/CMC composite electrode.

Source: Toner, M., Buettner, H. (1998). Microfabrication in biology and medicine. Biotechnology Progress, 14(3), 355–355. https://doi.org/10.1021/bp980203f

Photoresist is a photosensitive polymer that reacts when exposed to ultraviolet (UV) light. Photoresists are broken up into two categories, positive and negative. Positive photoresist are polymers that become weak when exposed to UV light. The weakened photoresist can then be dissolved in a developer solution leaving the desired pattern on the substrate. Figure 3.1 depicts the results of using a positive photoresist. Negative photoresists work in the opposite fashion. When a negative photoresist is exposed to UV light it become stronger and all unexposed photoresist can be dissolved away.

After spin coating the substrate with photoresist, the mask is held over the sample and UV light is transmitted through the mask exposing all uncovered photoresist. A developer solution is then utilized to dissolve any unwanted photoresist. Photolithography can also be done without a mask in which a tool is needed to directly write the pattern onto the photoresist. The most common tool for mask-less photolithography is known as a Heidelberg DW66+. In this study both standard photolithography and mask-less photolithography were attempted, but the mask less photolithography showed better results and thus utilized for all final sample fabrication.

3.2.2 Multi-beam Optical Sensing

Multi-beam optical sensing (MOS) is an experimental technique that utilizes laser beams to measure the in situ curvature change of an elastic substrate. This is done by first splitting a single laser beam into a two-dimensional array of laser beams. The initially generated laser beam is passed through a series of etalons, which splits the initial beam into an equally spaced two-dimensional array of beams. The array of laser beams is then projected and reflected off the backside of an elastic substrate. The reflected beams are captured with a high-resolution CCD camera and the centroid of each reflected laser beam is tracked with image processing software. Since laser

beams are tracked in two orthogonal directions, a two-dimensional measurement of the curvature is made. Furthermore, measurements made with MOS is inherently less sensitive to vibrations of the sample because the simultaneous tracking of the array of lasers. A schematic of the MOS system can be seen in Figure 3.2.

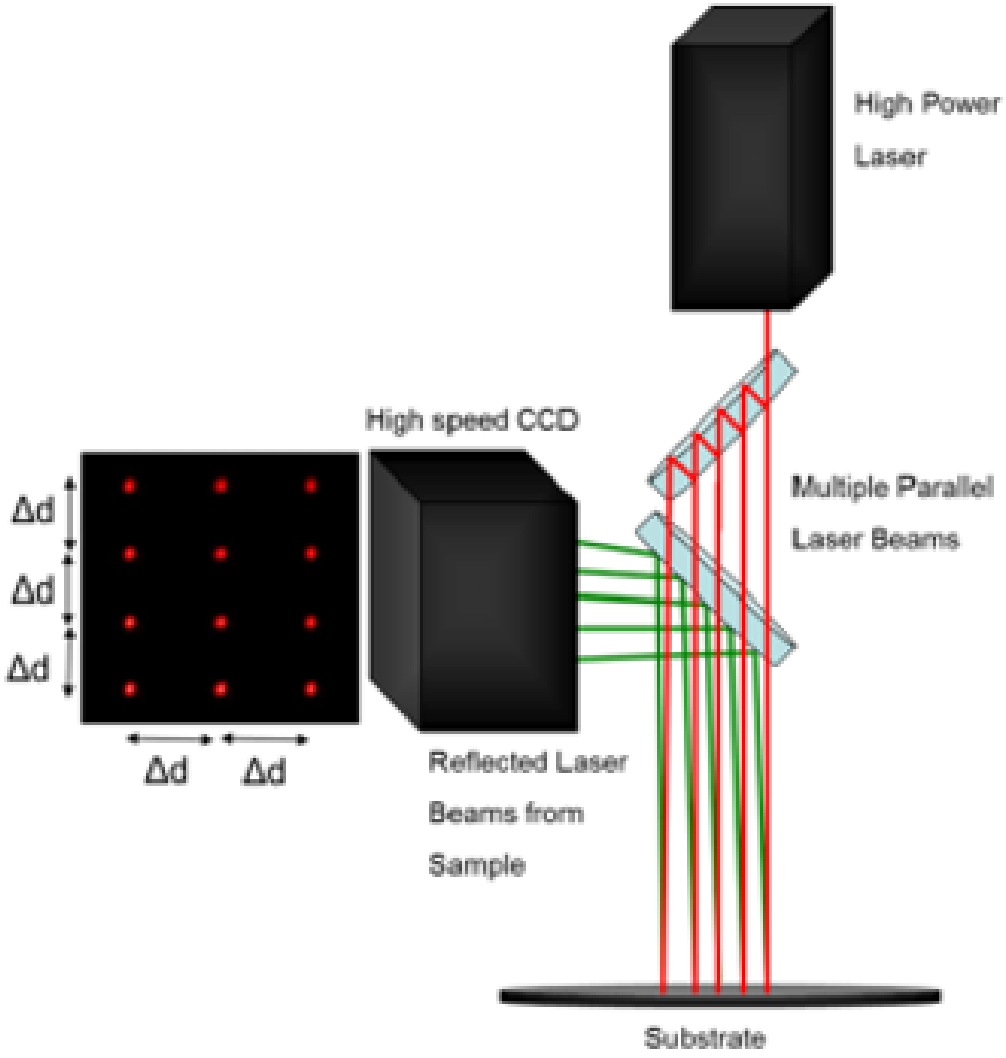

Figure 3.2 Schematic of the Multi-beam optical sensor (MOS).

Source: https://www.k-space.com/wp-content/uploads/MOS_Product_Specs.pdf

The curvature of the sample is calculated by measuring the relative change in position of the centroids of each laser beam and then utilizing the following equation

$$\kappa = \frac{d - d_o}{d_o} * \frac{1}{A_m} \tag{3.1}$$

Where κ is the curvature of the substrate, d is the current distance between laser spots, d_o is the initial distance between laser spots, and $A - m$ is the mirror constant of the MOS system. The mirror constant is a constant value that depends on the length in which the lasers must travel as well as the incident angle in which the beams are reflected off the substrate. The mirror constant is experimentally found by first establishing a flat reference. This is done by measuring the curvature of a flat reference mirror. A curved reference mirror with known curvature is then utilized and the mirror constant is then measured.

The stress of a function of the film thickness can then be interpreted by utilizing the following equation

$$\sigma * h_f = \frac{E_s h_s^2 \kappa}{6(1 - \nu_s)} \tag{3.2}$$

Where σ is the stress in the film, h_f is the film thickness, E_s is the elastic modulus of the substrate, κ is the curvature of the substrate, and ν_s is the Poisson ratio of the substrate.

3.2.3 Pillar Fabrication

Double side polished (111) Si wafers (50.8 mm diameter, 0.5 mm thickness, N-type doped with As, R: 0.005-0.05 ohm.cm) were purchased from MTI Corporation. A regular pattern of circles was generated using Layout Editor software. The diameter of the circles was 10 μm and the pitch between circles was 2 μm. A 51 mm by 51 mm

square of these circles was then created such that it would fully encompass the 50.8 mm diameter Si wafer. The Si wafers were then brought to the Princeton Institute for the Science and Technology of Materials (PRISM) facility for photolithography.

The first step in the photolithography process was to apply a layer of photoresist onto the Si wafer. The photoresist used was AZ 1518. AZ 1518 is a positive photoresist which means that as it is exposed to ultraviolet (UV) light the polymer would react such that the polymer chains are weakened and thus the exposed photoresist can be easily dissolved in a developer solution. This means that after the photoresist is exposed to UV light and developed, an exact copy of the circles created in Layout editor would remain while area between the circles would be left clean of photoresist. Since the height of the pillars was required to be 10 μm, the layer of photoresist had to be more than 1 μm thick. This is because the AZ 1518 is removed during the etching process at a rate of 1 μm for every 10μm of Si removed. Spin coating a thick layer of photoresist directly onto Si wafers typically results in uneven films due to streaks cause by bubbles that form during the spin coating process. To alleviate this issue the surface of the Si wafer was treated in order to improve the adhesion between photoresist and Si which prevents the uneven films from occurring. To improve the adhesion between SI and photoresist a thin layer of bis(trimethylsilyl)amine (HMDS) was deposited onto the surface of the wafer.

HMDS was applied to the wafer by first dehydrating the wafer to remove any residual moisture trapped within the surface of the wafer. Removing the residual moisture on the surface of the wafer allowed for the HMDS to bond directly with the native oxide layer on the Si wafer. The HMDS layer applied was thinner than the oxide layer on the wafer. With the HMDS applied, the AZ 1518 was then spin coated onto the wafer at 4000 RPMs for 40 s. This allowed for a layer of photoresist that was over 1 μm thick to be created. After spinning the resist, the wafer was transferred to a hot plat set to 95°C and baked for 60 s.

The wafers were then brought to a Heidelberg DWL66+ to expose the wafers to UV light. The Heidelberg operates by directly writing a pattern onto the surface of the photoresist making it a mask-less photolithography technique. Prior to exposing the wafer to UV light, the desired pattern was uploaded to the Heidelberg computer and the standard 10 mm write head was used. The write head determines the resolution of the pattern and dictates the smallest possible feature size that can be created. The parameters used for the exposure were 95% UV light intensity coupled with 10% focus. No offset in the X or the Y directions were needed. The pattern was centered with the center of the wafer such that the 51 mm square fully encompassed the wafer. Exposure was then conducted for 20 mins.

Once the Heidelberg finished writing the pattern onto the wafer, AZ300MIF developer was used to remove the exposed photoresist. This process involved soaking the wafer in developer for 60 s when gently stirring the wafer in the developer to propagate the removal of exposed photoresist. An optical microscope was then utilized to verify that the circular pads of photoresist were properly created, while also verifying that all exposed photoresist was removed. The wafers were then placed in wafer carriers and brought to the Center for Functional Nanomaterials (CFN) at Brookhaven national Lab for Si etching and metal deposition.

Prior to etching the wafer were de-scummed to remove any residual HMDS as well as any residual photoresist. This process was not initial conducted which resulted in uneven walls around the etched pillars. SEM images were taken of the photoresist pads prior to etching and it was found that there was thin layer of "scum" or residual photoresist at the edges. The layer of scum influenced the final geometry of the pillars and thus had to be removed. This was done by placing the wafer into an O_2 plasma oven for 60 s. This process removed the nanoscale residual photoresist that was present around the edges of the photoresist pad.

An Oxford-F DRIE etcher was then utilized in which a cryo-etch procedure was run for 4 minutes to ensure a pillar height of 15 μm. The cryo-etch procedure involved lowering the temperature of the etcher to -100 °C. Fluorine gas was then utilized to remove any Si that was not covered with photoresist. Once the etching process was over, O_2 plasma was utilized to remove the photoresist that was present on the top surface of the now etched pillars. The wafer was removed from the etcher and cooled only to then be cleaned with acetone and IPA. The geometry of the etched pillars was then characterized with SEM images.

After etching, a 5 nm layer of titanium and a 200 nm layer of copper were deposited on the backside of the wafer using a Lesker sputterer. This was done by adhering the etched wafer inside the sputterer and bringing the tool to ultra-high vacuum. The Ti and Cu targets were the sputtered with O_2 plasma to coat the backside of the wafer. The time in which the samples were sputtered corresponded to the sputter rate of those materials. Ti and Cu were sputtered onto the backside of the wafer in order to uniformly distribute current throughout the Si wafer during electrochemical cycling. Ti was utilized as an adhesive layer due to poor adhesion between Cu and Si. The Cu acts as current collector and was imperative for the proper cycling of the wafers. Etched wafers were initially cycled without the metal layers on the backside, which resulted in a poor connection and thus failure of the electrochemical tests. The addition of the Ti / Cu layer improved the current distribution and allowed for proper electrochemical testing.

Polymer binder was then added to the pillared side of the wafer. PVDF (534,000 Mw) was purchased from Sigma-Aldrich and mixed with 1-methyl-2-pyrrolidinone (NMP) from Sigma-Aldrich to make a 6 wt% solution of PVDF in NMP. The PVDF solution was then spun coat onto the etched wafer at 1000 RPMs for 30 s to distribute the polymer evenly between the pillars. The sample was then vacuum heated at 70 °C for 24 hrs in an Ar environment. A 5 wt% solution of CMC was then made by

mixing CMC (Mw 250,000) with a pH 3 solution of acetic acid in deionized water. The solution was first coated onto the wafer with a spatula such that the entire wafer was uniformly covered in the CMC solution prior to spin coating. The wafer was then spun at 1000 RPMs for 30s and vacuum dried at 70°C for 24 hrs in an Ar environment. The polymer binder bridges that formed between the pillars where characterized by SEM analysis.

3.2.4 Beaker Cell Fabrication

Prior to cycling, the pillared wafers are vacuum dried in Ar for 24 hrs at 70°C to ensure that any residual moisture is removed. Along with the wafer, Celgard is also vacuum dried to remove any possible moisture in the material. Once the wafer and Celgard are dried, they are inserted into an MBraun Glovebox, which maintains an Ar environment with O_2 and H_2 below 5 ppm.

Unlike Chapter 2, the electrochemical cycling was conducted in a custom made beaker cell opposed to a coin cell configuration. This was done such that in situ stress measurements could be taken as the cell electrochemically cycled. A schematic of the custom beaker cell is shown in Figure 3.3 which also highlights how the MOS lasers reflect off the wafer.

To assemble the beaker cell configuration, a disc of lithium was first cut out and a copper wire was attached to it. The lithium disc acted as a reference electrode in this experimental set up. The Celgard was then placed over the Li disc and 2 mL of electrolyte (1 molar LiPF6 in 1:1:1 vol. ratio of EC:DC:DMC) was added to the system. The pillared wafer was the added to the beaker cell and an electrical connection was made by connecting a Cu wire to the wafer with a Cu clip. A steel cap with a glass window was then screwed onto the top of the beaker cell with a gasket between the steel and the Teflon to ensure a tight seal.

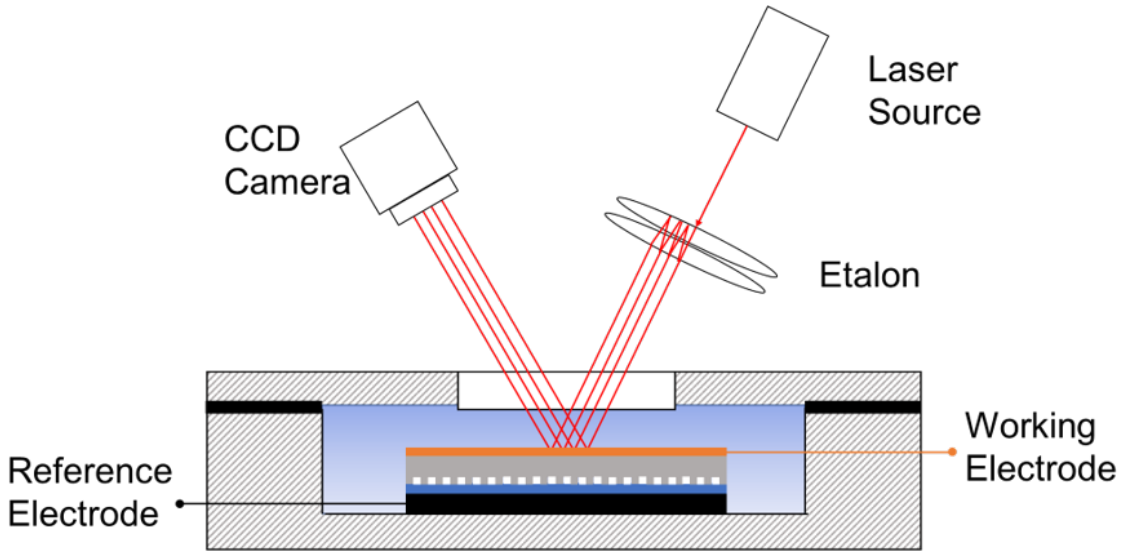

Figure 3.3 Schematic of the custom made beaker cell utilized in this study. The housing of the beaker cell was made of Teflon, while the cover was made of steel. In the cover was a glass window which allowed the laser beams of the MOS system to project onto the backside of the pillared wafer.

3.2.5 Electrochemical Testing

A galvanostatic study was conducted by applying a constant current density of 25 μA/cm2. Prior to cycling the top surface of the wafer was imaged using a digital camera, and the area was calculated using ImageJ software. The voltage cutoffs for the test were 0.05 V vs. Li/Li+ for lithiation and 1.2 V vs. Li/Li+ for delithiation. The cell was then cycled 2.5 times where each (de)lithiation was set for 25 hrs. After cycling, the cell was then disassembled and rinsed with DMC and SEM analysis was conducted to characterize the change in volume due to electrochemical cycling.

3.3 Results and Discussion

After developing the desired patterned of circles onto the first set of Si wafers, an optical microscope was used to verify that all residual photoresist was removed. The image taken from the optical microscope can be seen in Figure 3.4.

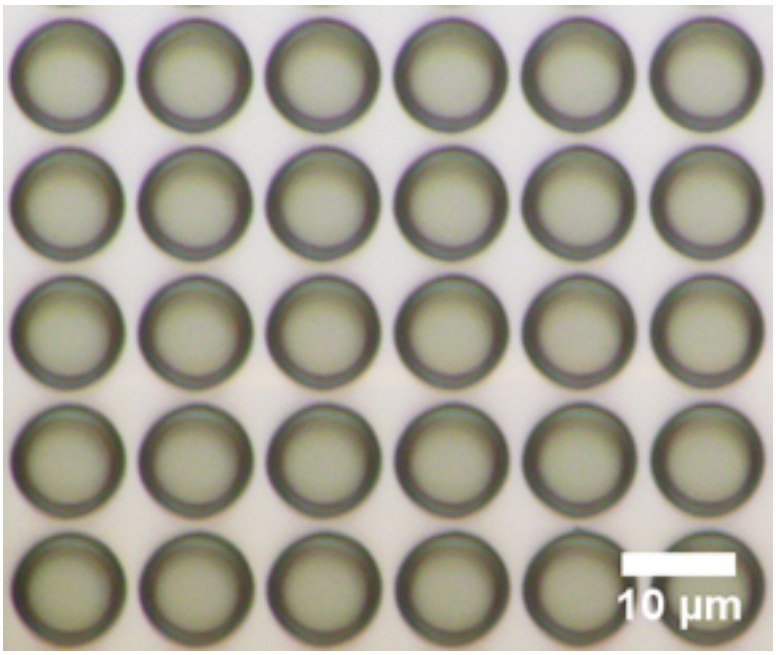

Figure 3.4 Photoresist pads after 60 s of developing.

The initial pads of photoresist seen in Figure 3.4 were properly sized and all residual photoresist was removed, so the samples were etched using a cryo-DRIE etching process. The etched wafers were then characterized using SEM. The geometry of a single pillar on an etched wafer can be seen in Figure 3.5. The pillars had undesirable geometry in which a "shell" structure could be seen wrapped around the pillars. Due to this result SEM images were then taken of developed photoresist pads in order to fully characterize the pad of photoresist at a much higher magnification than the optical microscope would allow.

From the SEM imaging it was found that there was considerable residual photoresist, or scum, around the edges of the developed pad. This result can be seen in Figure 3.6A where there is a dark region around the pad of photoresist. This region created the shell structure around the pillars after etching. To alleviate the issues a 60 s de-scumming procedure was conducted. SEM images were taken after de-scumming, which can be seen in Figure 3.6 B. The 60 s de-scumming process

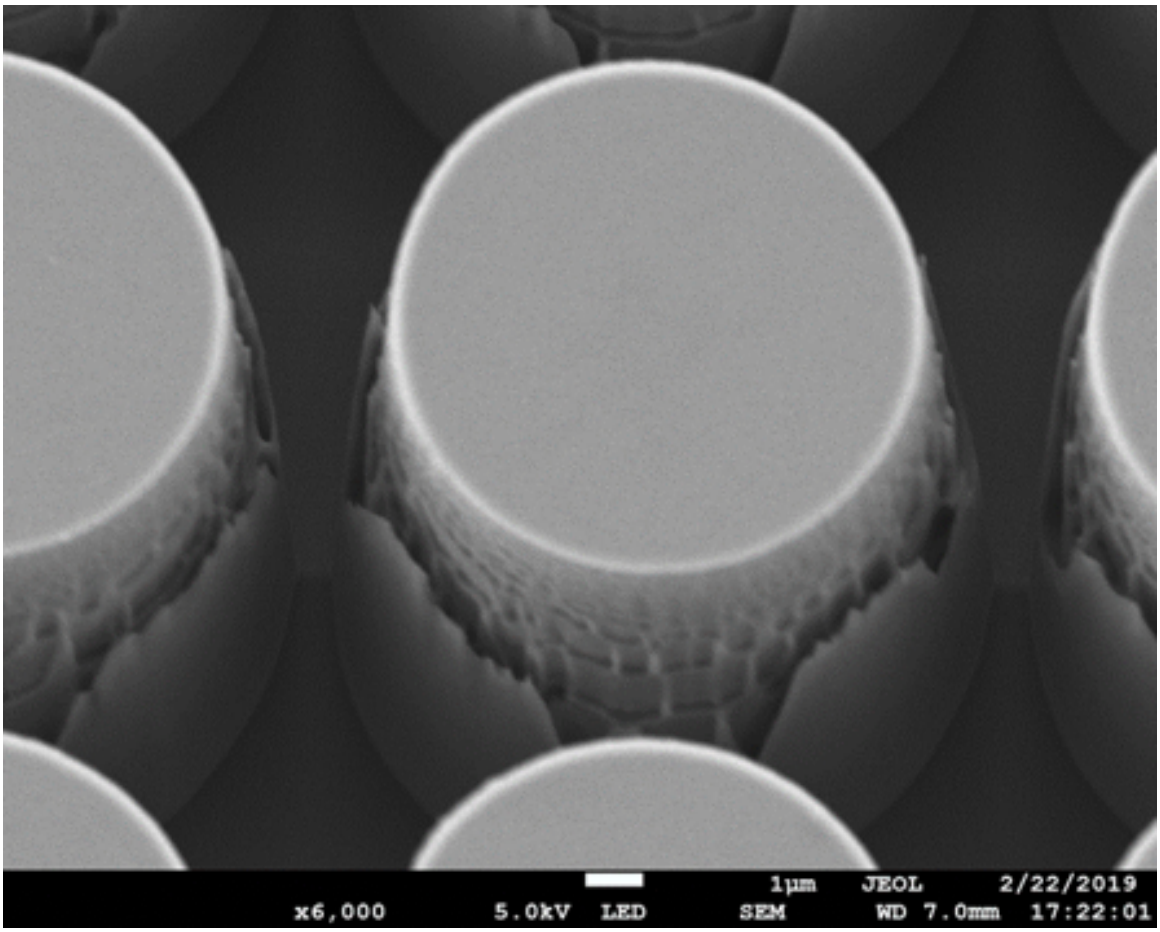

Figure 3.5 Etched pillar without de-scumming process. A "shell" can be seen around the pillar.

removed all the scum around the phot resist pad. This result allowed for the creation of pillars with proper geometry.

SEM images of the pillars created after utilizing a 60 s de-scumming process can be seen in Figure 3.7. Figure 3.7 A shows a field of micro pillars of Si etched onto the Si wafer. Higher magnification images were then taken in order to properly measure the geometry of the pillars. Figure 3.7 B shows a high magnification SEM of a single pillar. The diameter of the pillar was 9.7 μm and the pitch between the pillars was measured to be 2 μm. The wafer was then tiled by 25° in order to see the side walls of the pillars, which is shown in Figure 3.7 C. Finally, SEM images were taken from the side to characterize the vertical walls of the etched pillars, as well as,

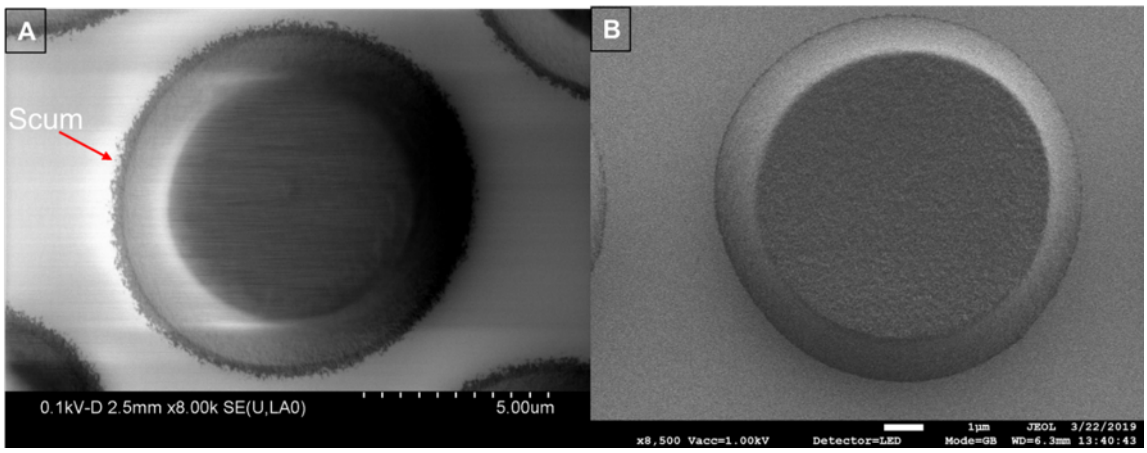

Figure 3.6 Photoresist pad before (A) and after (B) de-scumming.

measure the height of the pillars after etching. Figure 3.7 D shows the side image of the etched pillars where the height was measured to be 15 μm and the wall were shown to be vertical with little to no tapering.

Once the pillars were able to be created with the desired geometry, electrochemical testing was conducted coupled with in situ curvature measurements. The pillared sample was cycled galvanostaticly without binder for 2.5 cycles in order to properly characterize the curvature change as the pillars expanded and contracted. The results of the galvanostatic testing can be seen in Figure 3.8 and the curvature measurements can be seen in Figure 3.9.

From Figure 3.8, the voltage curves associated with lithiation and delithiation can be seen. During the first cycle of lithiation the sample's potential drops to 0.1 V and a voltage plateau was observed. This voltage plateau corresponds to a moving phase boundary which was in accordance with the observed behavior of crystalline Si in the literature. The delithiation of the sample was also characteristic of a crystalline Si wafer, and thus it was confirmed that the pillared sample was properly electrochemically cycled.

From Figure 3.9, the curvature behavior of the sample can be understood. Initially there is no curvature change as the cell lithiates. During this time the

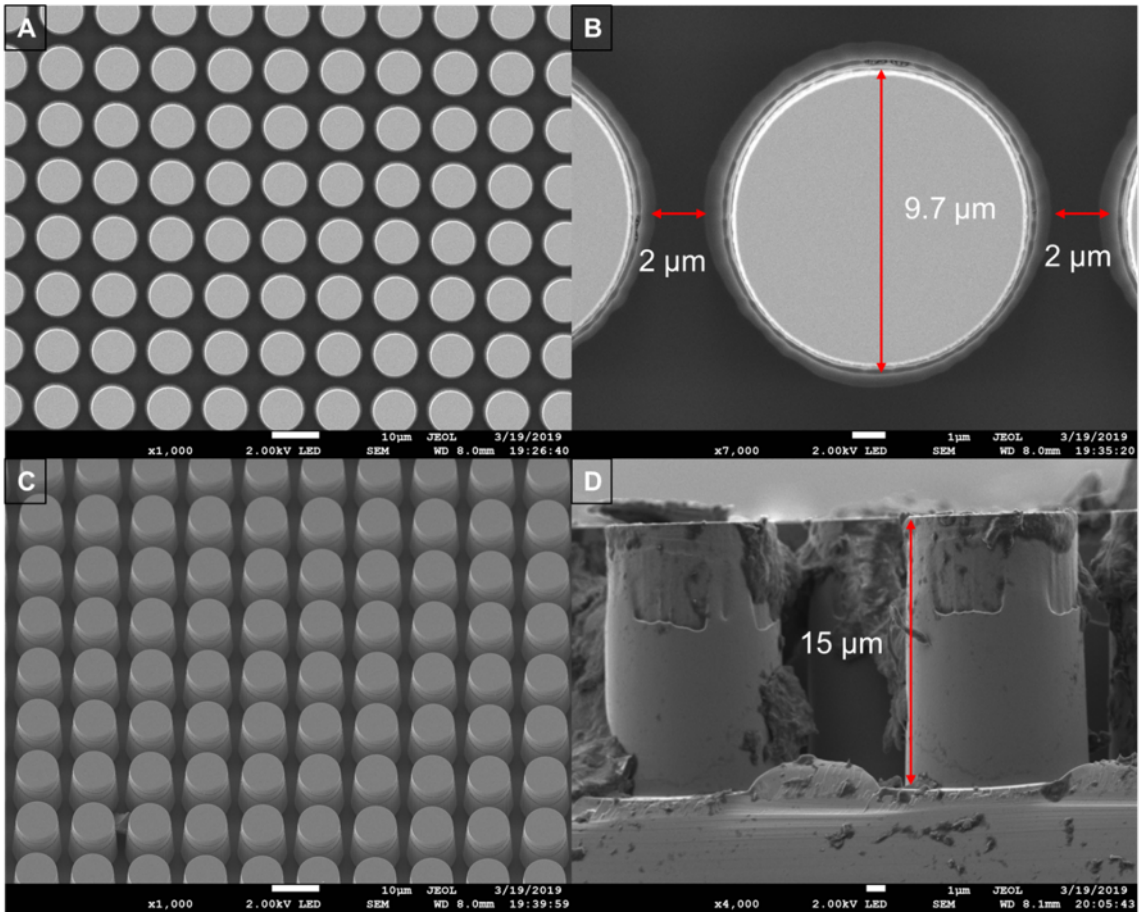

Figure 3.7 Si pillars after etching. Top views (A-B) show the diameter of the pillars to be 10 μm and the pitch between them to be 2μm. SEM Images were taken with a 25 ° tilted view (C) to show the side walls of the etched pillars. SEM images take on the side (D) of the pillars were taken to measure the height after etching which was 15 μm.

pillars are not touching but are expanding as they react with lithium. After roughly 15 hours of lithiation, there is sharp increase in compressive stress associated with the touching of the pillars due to volume expansion. The observed compressive stress increases until the time constant imposed on the lithiation step of the galvanostatic cycle was completed. During delithiation, the volume of the pillars was reduced which results in a sharp increase in tensile stress that occurs over the course of only a few hours. After this point, the continuation of a liner increase in tensile stress was observed until the end of delithiation.

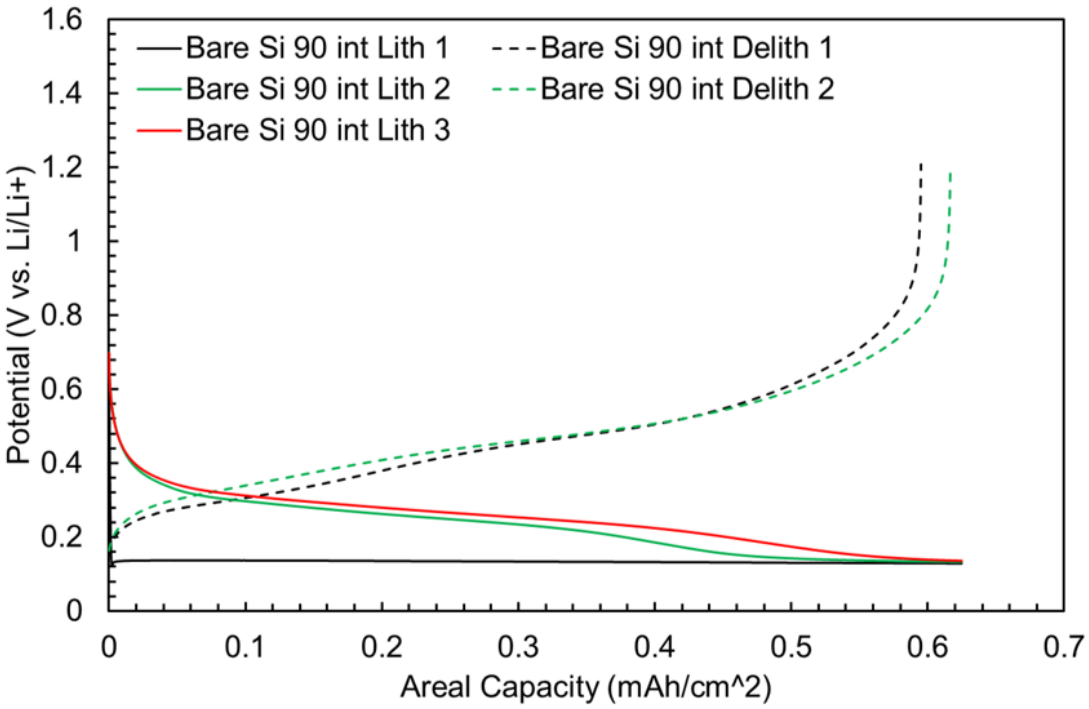

Figure 3.8 Results of the galvanostatic testing done to the bare pillared Si wafer.

During the second lithiation there is an unexpected increase in tensile stress over the course of a few hours. The reason for this behavior is not known, but it can be hypothesized that it is due to the fusing of touching pillars. Subsequent curvature behavior was then observed to be like that of the wafer during the first lithiation and delithiation. SEM analysis was then conducted on the wafer after its third lithiation to fully understand the volume expansion that occurred, as well as, to verity the touching of pillars.

SEM analysis was conducted in three different areas of the cycled wafer as illustrated in Figure 3.10. From Figure 3.10 SEM analysis was conducted in the middle of the wafer, and at the two extreme ends of the wafer. Point 1 represents the location in which the connection was made to the wafer, point 2 represent the middle of the wafer, and point 3 represents the area furthest away from the connection. These three points were chosen to verify that the morphology of the pillars were similar over the entirety of the wafer.

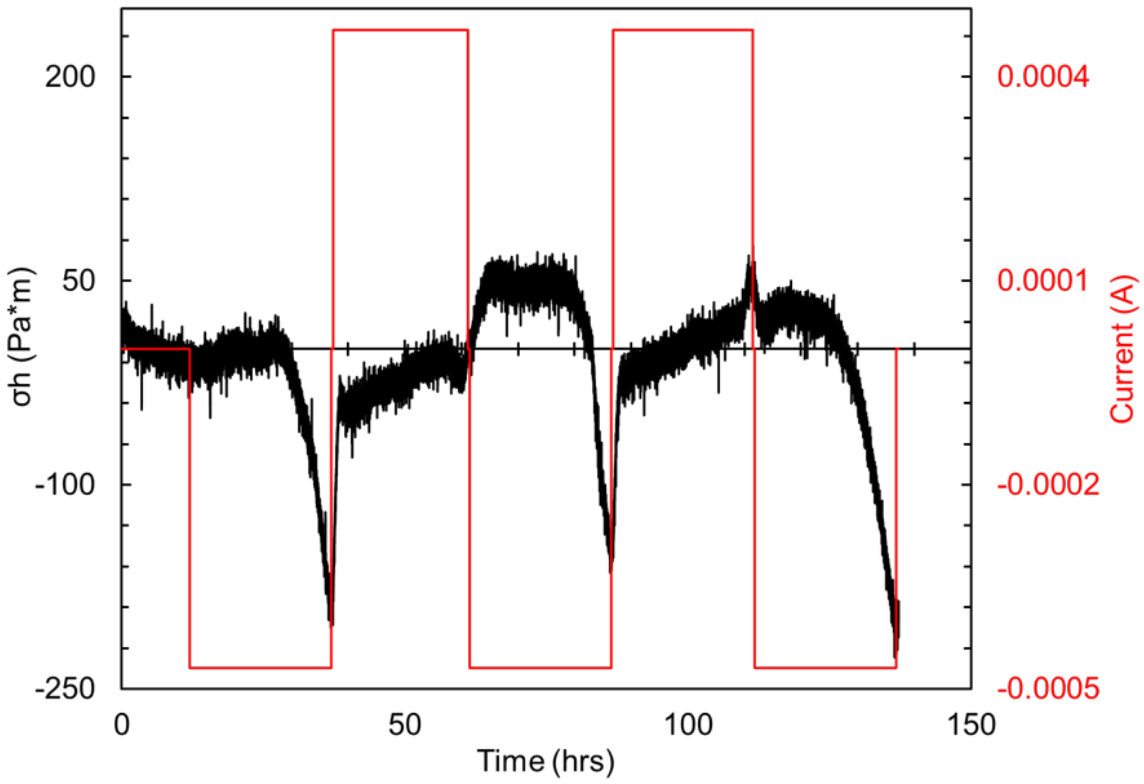

Figure 3.9 Stress response of the bare Si wafer after 2.5 cycles of galvanostatic testing. The applied current is also shown in red.

Figure 3.11 shows the images captured with SEM at each of the three point. At point 1 (Figure 3.11A and 3.11B) the pillars were touching after the third lithiation. There was also substantial volume expansion of the outer walls of the Si pillars. Interestingly there was no observed volume expansion of the top surface of the wafer. This was due to the anisotropic lithiation of Si in which the Si has preferred directions in which lithiation is favorable. Goldman et al. showed this behavior by etching bars of Si into a (111) crystal Si wafer. The side walls of the etched bars had 110 planes, while the top surface had 111 planes. During electrochemical cycling the side walls expanded, while the top surface did not. This result showed that the lithiation of crystal Si was preferred on the 110 plane. In this study, similar crystal wafers were

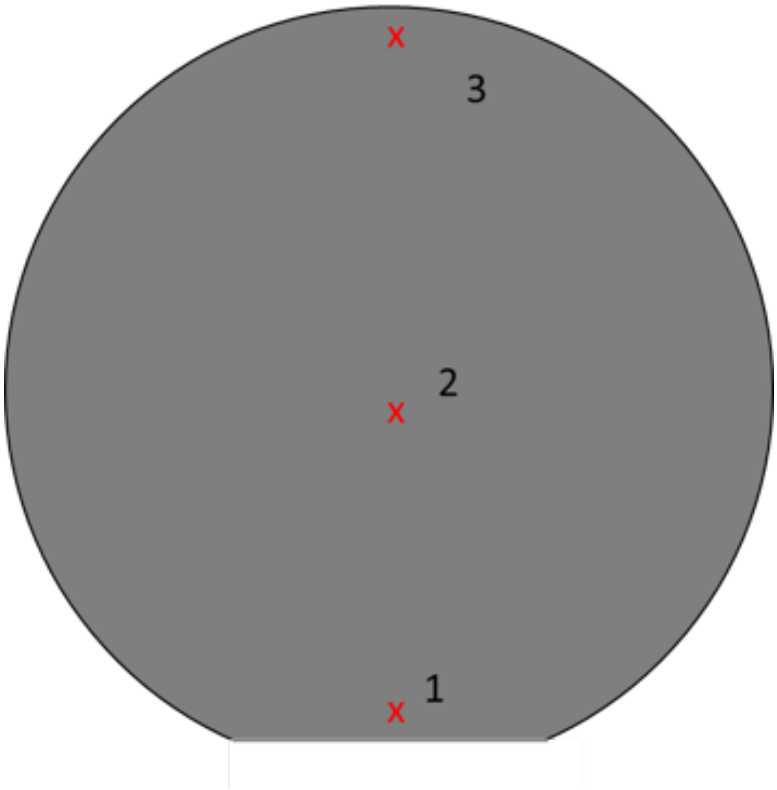

Figure 3.10 Location of SEM analysis conducted on the cycled wafer.

etched, thus similar which explains why the tops of the pillars did not experience any volume change during cycling.

At point 2 (Figure 3.11 C and 3.11D) similar volume expansion of the side walls of the pillars as well as touching of the neighboring pillars was observed. Cracking of the pillars was observed at both points. At point 3 (Figure 3.11E and 3.11F) there was an extreme amount of fracture. The fracture of the Si was predominantly at the interface between amorphous lithiated Si and bulk crystal Si.

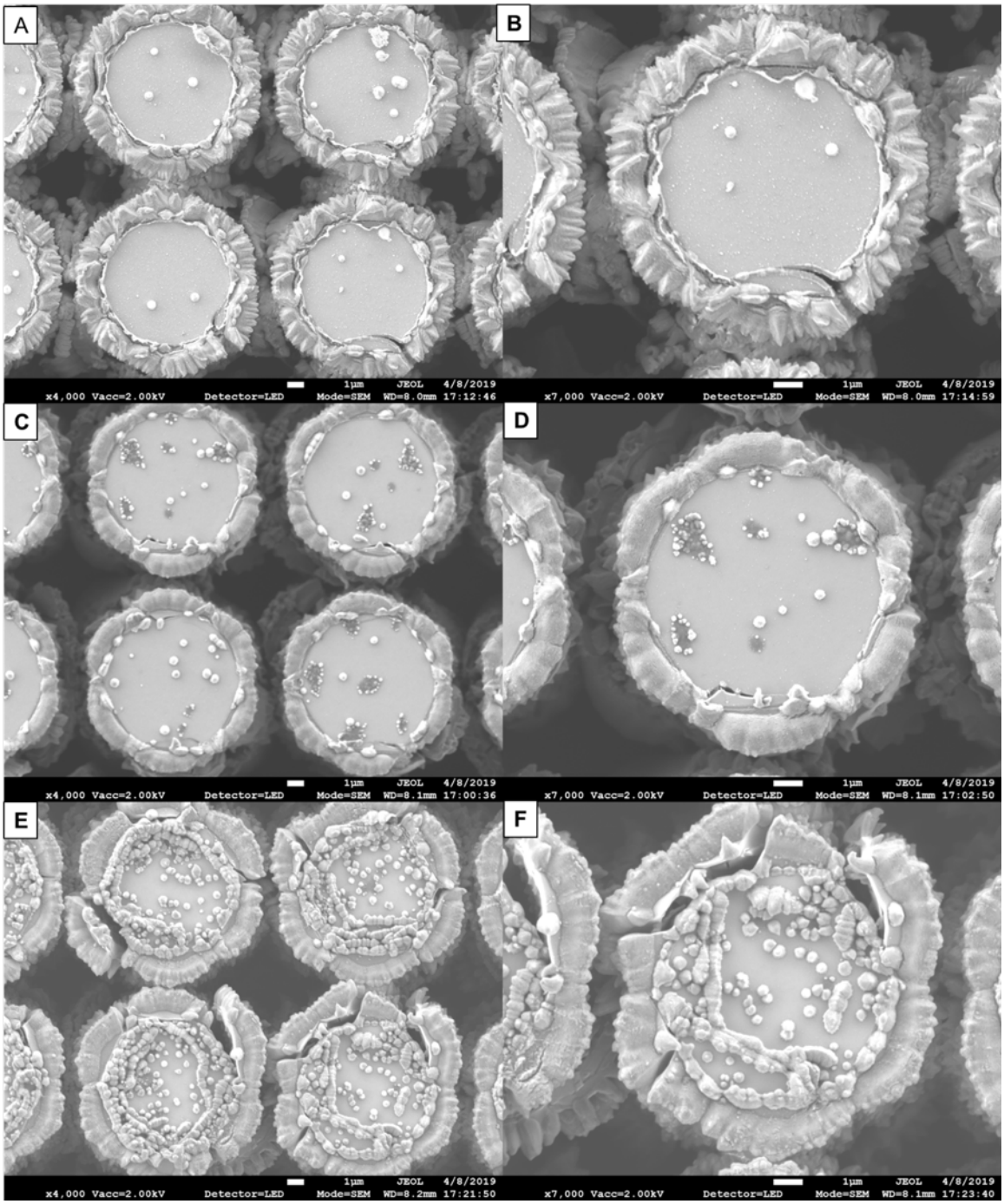

Figure 3.11 SEM Images taken at location 1 (A-B), location 2 (C-D), and location 3 (E-F). Cracking can be seen in the pillars.

With the geometry of the cycled Si pillars properly characterized after electrochemical cycling, both PVDF and CMC were added to the sample. Prior to cycling the formation of binder bridges between pillars was characterized using SEM analysis

shown in Figure 3.12. Both PVDF (Figure 3.12A and 3.12B) and CMC (Figure 3.12C and 3.12D) show binder bridges that connect all pillars together. This formation of binder bridges between the Si pillars, coupled with the proper electrochemical cycling of the bare Si pillars helped to validate the use of this idealized composite electrode.

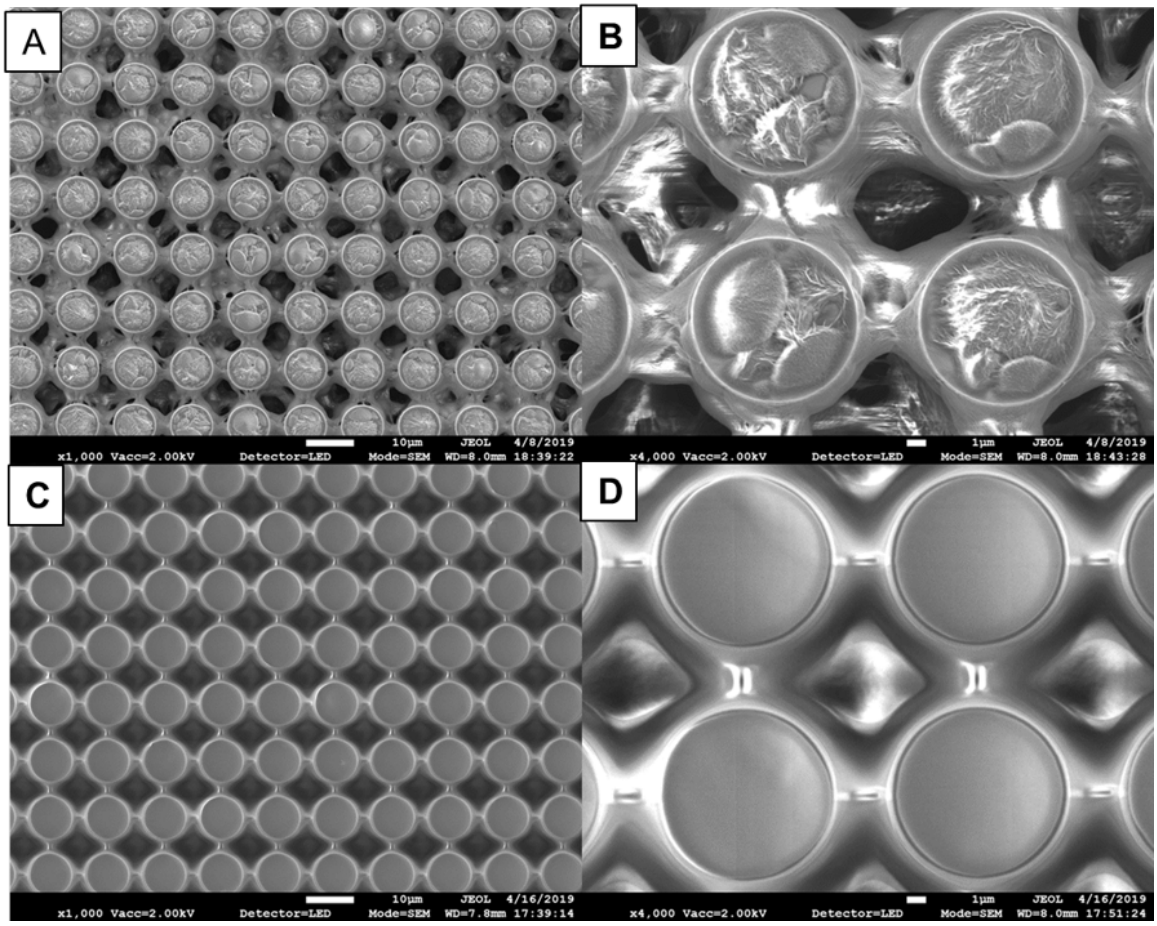

Figure 3.12 SEM Images of PVDF (A and B) binder bridges between Si pillars and CMC (C and D) binder bridges between Si pillars.

The samples were then cycled with both PVDF and CMC added. The resulting voltage curves of both PVDF and CMC can be seen in figure 3.13. From the results of the electrochemical cycling not only did the PVDF and CMC samples behave similar to the bare Si sample, but they also behaved similarly to each other. This was an expected result after it was observed in Chapter 2 that the presence of the binder did

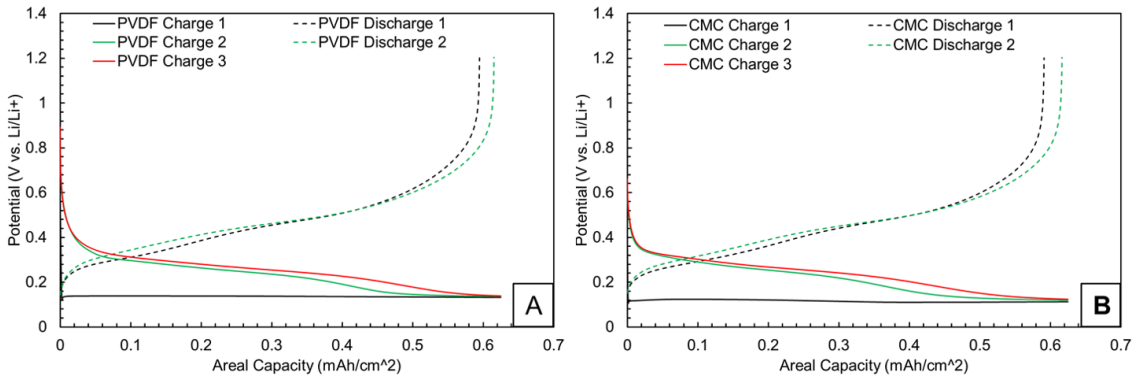

Figure 3.13 Voltage curves of PVDF (A) and CMC (B) after 2.5 galvanostatic cycles.

not affect the kinetics or the electrochemical response. These results help to further verify the proper lithiation of the pillars.

Unfortunately, there were issues with gathering the curvature data of the PVDF and CMC samples. During lithiation and delithiation, the curvature the wafer experienced was so great that it caused the lasers of the MOS system to move out of the area designated for taking measurements. The CMC sample lost almost all its curvature data, but the curvature data of the PVDF sample was enough to make some general observations. The curvature data of the PVDF sample can be seen in Figure 3.14. Similarly to the bare Si sample, there is initially no change in curvature of lithiation occurs. After 12 hours of lithiation there is a non-linear increase in compressive stress followed by a linear region of compressive stress, which occurs after 16 hours. The observed non-uniform stress was most likely due to the presence of the PVDF. Similar behavior was observed for all subsequent lithiation cycles. All data that was lost encompassed the delithiation of the sample, thus the behavior of the sample during delithiation was not able to be understood. After 2.5 galvanostatic cycles, SEM analysis was conducted. Much like the bare Si sample, three areas were analyzed to verify uniform lithiation.

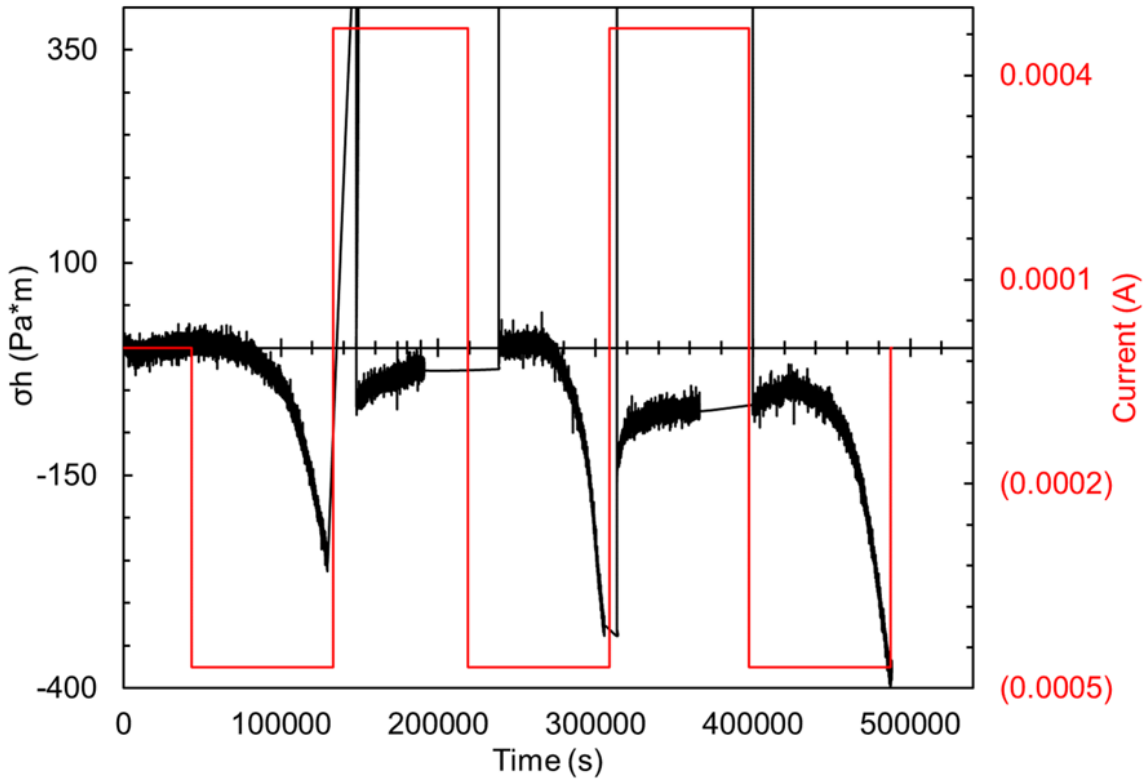

Figure 3.14 Stress response as a function of film thickness of a pillared Si sample with PVDF binder bridges. Some data was missing due to issues with curvature measurements, which resulted in gaps within the data.

The results of the SEM analysis showed that all three locations had similar geometries. That characteristic geometry is shown in Figure 3.15 in which both top views (3.15A and 3.15B) and tilted views (3.15C and 3.15D) were taken so see if fracture or touching occurred. From the SEM images it was observed that no touching occurred, as well as no cracking. From these results it can be conclude that the PVDF constrained the pillars such that fracture did not occur. Furthermore, the presence of the binder altered the final geometry of the pillars when compared to the sample without PVDF.

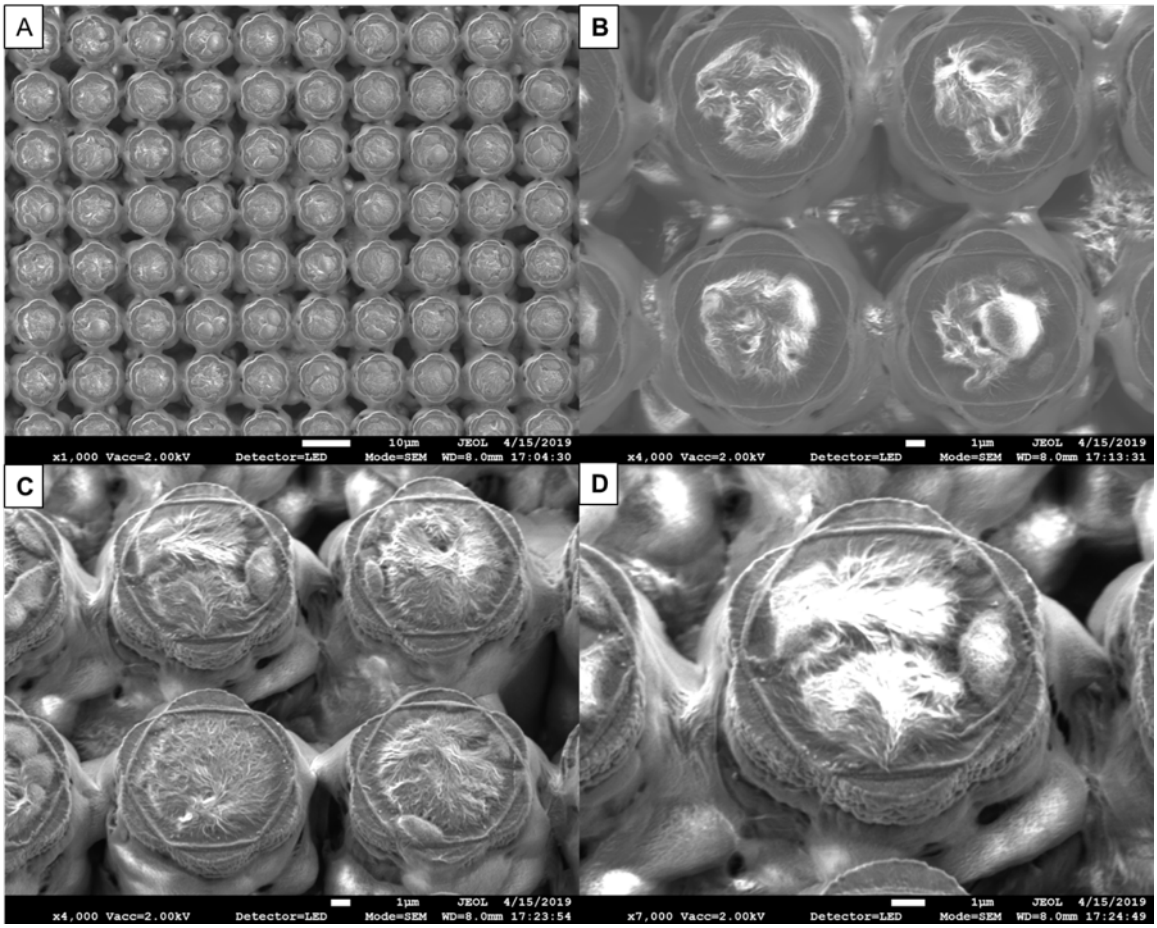

Figure 3.15 SEM images of cycled pillars with PVDF binder bridges. Top view of the sample (A and B) shows a "flower" pattern after 2.5 galvanostatic cycles. 25° tilt images (C and D) shows the structure of the outer wall of the pillars.

3.4 Conclusions

A microfabricated anode with idealized geometry was created to emulate the binder / particle interactions in a composite anode. Photolithography coupled with cryo-DRIE etching was utilized to etch a field of micropillars into a crystal Si wafer. The sample was then electrothermally cycled while curvature measurements were taken. The results of the curvature measurements were in accordance with the behavior of cycled crystalline Si as reported in the literature. SEM images of the cycled pillars showed that after 2.5 galvanostatic cycles, the side walls of the pillars expanded, while the top surfaces of the pillars did not. Touching of the pillars was also recorded.

Both PVDF and CMC were added to the sample to create binder bridges between the Si pillars. Both samples were then galvanostaticly cycled but, due to excessive curvature, the data was not properly recorded. The electrochemical cycling however did show that the pillars were lithiated properly but touching of the pillars was not seen in the PVDF sample. SEM imaging of the CMC sample was not completed.

The results of this study helped to verify the use of the idealized anode geometry. The Si pillars electrochemically cycled resulted in characteristic voltage curves. Binder bridges were then created between the pillars using both PVDF and CMC. To properly interpret the stresses at the particle level between the Si and binder a FEA model is needed to properly model the expansion of Si, while also modeling the response of the constrained polymer binder.

CHAPTER 4

CONCLUSIONS AND FUTURE WORK

4.1 Conclusions

The following conclusions were drawn from each chapter. In Chapter 2 thin films of PVDF and CMC were spun coat onto bare Si wafers and electrochemically cycled. The presence of the binder films did not alter the kinetics of the lithiation of Si, and characteristic CV curves of Si were observed. XPS analysis was conducted on the bare Si sample and showed that a characteristic SEI layer was formed. XPS analysis on PVDF showed that SEI did not form on the surface but did form inside the binder due to its ability to absorb electrolyte. XPS analysis of CMC showed that SEI formed on the surface of the binder, although it was not like the characteristic SEI formed in the Si sample. XPS further showed that SEI did not form within the binder. These XPS results fully characterized the location of SEI in PVDF and CMC, which has not been understood previously.

In Chapter 3 a field of Si micro pillars were etched into a Si wafer and electrochemically cycled. The volume expansion during cycling was enough to cause the pillars to touch when fully lithiated. Curvature measurements and stress estimations were made from the cycled bare Si sample with pillars. The addition of both CMC and PVDF allowed for the formation of binder bridges between Si pillars. Electrochemical cycling of the binder bridge samples was conducted but curvature measurements could not be made due to the large curvature change.

4.2 Future Work

In this thesis the interactions between polymer binder and Si were investigated. This was done by creating a sample capable of emulating the complex geometry of a composite anode. The sample was also able to emulate the binder bridges found

within a composite electrode. In order to further the understanding of the binder particle interactions a finite element model is needed. The model should be able to accurately infer the stresses generated within the polymer binder as electrochemical cycling occurs. This can be done by cycling the idealized composite sample created in this thesis and utilizing both the curvature measurements as well as the observed volume expansion of the pillars.

APPENDIX A

PVDF DEGRADATION DUE TO AR-ION SPUTTERING

Both Figure A.1 and A.2 show the degradation of PVDF due to Ar-ion sputtering. Figure A.1 shows the degradation of the C1s region in which the C-F peak associated with PVDF is completely degraded after only 1 30s sputter. The C-C peak associated with the PVDF also experiences a shift in BE, which is associated with a chemical degradation. Figure A.2 shows the chemical degradation of the F1s region. Again, the single peak associated with the PVDF film is almost completely removed after only one 30s sputter.

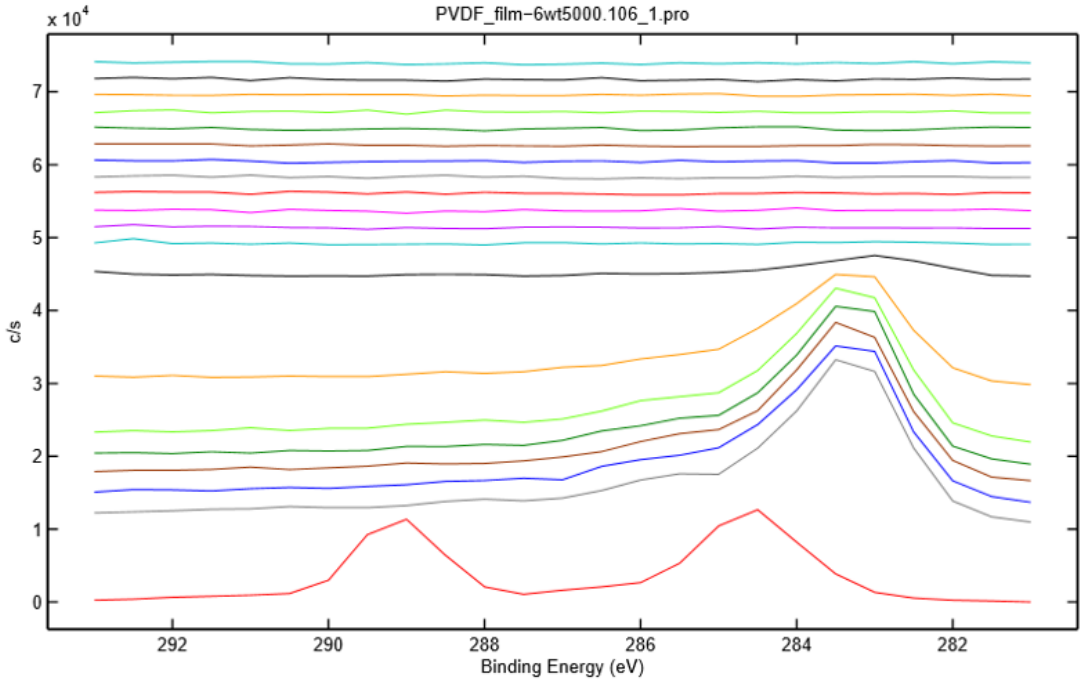

Figure A.1 Degradation of the C1s region of PVDF after Ar-ion sputtering.

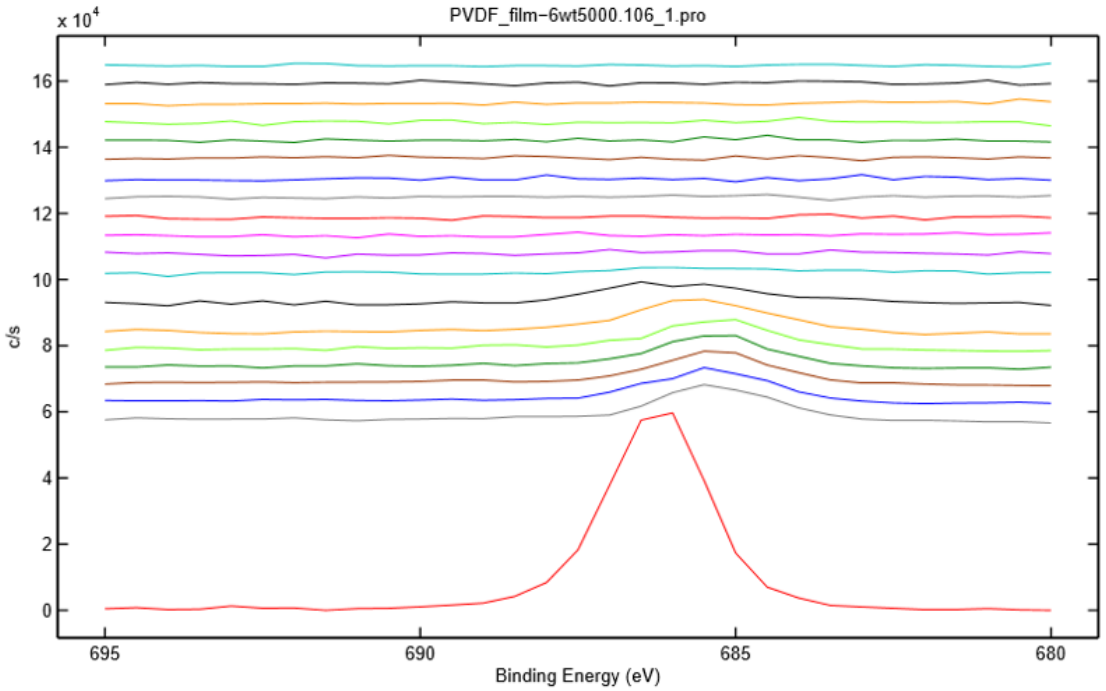

Figure A.2 Degradation of the F1s region of PVDF after Ar-ion sputtering.

APPENDIX B

XPS ANALYSIS CONDUCTED WITHIN THE BINDERS AND AT THE BINDER / SI INTERFACE

This section shows the peak parameters of both PVDF and CMC after C-60 ion milling. Table B.1 shows the peak parameters of PVDF which was analyzed within the binder and Table B.2 shows the peak parameters of PVDF at the binder / Si interface.Tables B.3 and B.4 show the peak parameters of CMC within the binder and at the binder / Si interface.

Table B.1 PVDF Peak Parameters of XPS Conducted Within the Binder

C1s				
Peak	BE	FWHM	Atm %	Assignment
1	285	1.7	11.2	C-H
2	286.1	1.4	6.4	C-C (PVDF)
3	287.6	2	3.9	C=O
4	289.7	1.9	1.9	Li2CO3
5	290.6	1.3	4.7	C-F (PVDF)
6	293	1	0.2	Shake-Up
O1s				
Peak	BE	FWHM	Atm %	Assignment
1	528.4	1.6	1.4	Li2O
2	531.2	1.8	12.6	Li2CO3/C-O
	532.8	2	1.2	C=O
F1s				
Peak	BE	FWHM	Atm %	Assignment
1	685	1.6	17.1	LiF
2	687.7	2	13.3	PVDF
Li1s				
Peak	BE	FWHM	Atm %	Assignment
1	54.1	2	4.7	Li2O
2	55.5	1.8	20.9	LiF/Li2CO3
Si2p				
Peak	BE	FWHM	Atm %	Assignment
1	96.3	1.5	0.1	Li-Si 2p3/2
2	96.9	1.4		Li-Si 2p1/2
3	101.1	2	0.1	Si 2p3/2
4	101.7	2		Si 2p1/2

Table B.2 PVDF Peak Parameters of XPS Conducted at the PVDF / Si Interface

C1s				
Peak	BE	FWHM	Atm %	Assignment
1	279.8	1.0	0.3	SiC
2	282.4	1.9	0.8	LiC
3	284.8	2.0	9.2	C-H
4	286.0	1.4	1.7	C-C (PVDF)
5	287.4	1.9	1.5	C=O
6	290.0	1.8	2.9	C-F (PVDF) /Li2CO3
O1s				
Peak	BE	FWHM	Atm %	Assignment
1	528.3	1.9	7.2	Li2O
2	531.2	2.0	16.8	Li2CO3/C-O
F1s				
Peak	BE	FWHM	Atm %	Assignment
1	685.0	1.7	10.1	LiF
2	687.5	2.0	3.1	PVDF
Li1s				
Peak	BE	FWHM	Atm %	Assignment
1	52.9	1.2	9.2	Li-Si
2	54.2	1.7	15.8	Li2O
3	55.5	1.7	14.9	LiF/Li2CO3
Si2p				
Peak	BE	FWHM	Atm %	Assignment
1	96.4	1.3	5.2	Li-Si 2p3/2
2	97.0	1.3		Li-Si 2p1/2
3	97.9	1.5	0.5	Si 2p3/2
4	98.5	1.5		Si 2p1/2
5	100.3	1.7	0.6	SiC 2p3/2
6	100.9	1.7		SiC 2p1/2

Table B.3 CMC Peak Parameters of XPS Conducted Within the Binder

C1s				
Peak	BE	FWHM	Atomic %	Assignment
1	284.8	1.9	40.4	C-H
2	286.4	1.1	8.1	C-O
3	288.1	2.0	11.0	O=C-O
O1s				
Peak	BE	FWHM	Atomic %	Assignment
1	530.9	1.9	13.8	C-O
2	532.7	1.7	6.2	CMC
3	535.5	2.4	5.3	Na Auger
F1s				
Peak	BE	FWHM	Atomic %	Assignment
1	683.5	1.3	11.6	NaF
2	685.2	1.5	2.1	LiF
Na1a				
Peak	BE	FWHM	Atomic %	Assignment
1	1071.1	1.6	16.5	Na-CMC

Table B.4 CMC Peak Parameters of XPS Conducted at the CMC / Si Interface

C1s				
Peak	BE	FWHM	Atomic %	Assignment
1	284.3	2.0	23.3	C-H
2	286.0	1.5	5.3	C-O
3	287.9	2.0	5.7	O=C-O
O1s				
Peak	BE	FWHM	Atomic %	Assignment
1	528.4	1.4	2.5	Li2O/ROLi
2	530.5	2.0	13.8	C-O
3	532.3	1.4	1.9	CMC
4	534.7	3.0	7.1	Na Auger
F1s				
Peak	BE	FWHM	Atomic %	Assignment
1	682.8	1.6	12.2	NaF
2	685.0	2.0	1.5	LiF
Na1a				
Peak	BE	FWHM	Atomic %	Assignment
1	1070.4	2.0	28.0	Na-CMC
Si2p				
Peak	BE	FWHM	Atomic %	Assignment
1	96.4	1.0	10.2	LiSi
2	97.0	1.0		
3	100.4	2.0	2.9	SiC
4	101.0	2.0		

REFERENCES

[1] J. S. Bridel, T. Azaïs, M. Morcrette, J. M. Tarascon, and D. Larcher. Key parameters governing the reversibility of Si/carbon/CMC electrodes for Li-ion batteries. *Chemistry of Materials*, 22(3):1229–1241, 2010.

[2] Michael C. Burrell and John J. Chera. Charge correction of the binding energy scale in XPS analysis of polymers using surface deposition of PDMS. *Surface and Interface Analysis*, 27(9):811–815, 1999.

[3] Libao Chen, Xiaohua Xie, Jingying Xie, Ke Wang, and Jun Yang. Binder effect on cycling performance of silicon/carbon composite anodes for lithium ion batteries. *Journal of Applied Electrochemistry*, 36(10):1099–1104, oct 2006.

[4] Zonghai Chen, L Christensen, and J R Dahn. A study of the mechanical and electrical properties of a polymer/carbon black binder system used in battery electrodes. *Journal of Applied Polymer Science*, 90(7):1891–1899, nov 2003.

[5] M. J. Chon, V. A. Sethuraman, A. McCormick, V. Srinivasan, and P. R. Guduru. Real-time measurement of stress and damage evolution during initial lithiation of crystalline silicon. *Physical Review Letters*, 107(4):1–4, 2011.

[6] Marine Corps and After Next. Naval Research and Development. *Nature*, 156(3964):472–472, oct 1945.

[7] Department of the Navy. The Navy Unmanned Undersea Vehicle (UUV) Master Plan. (November):127, 2004.

[8] Z. Karkar, D. Guyomard, L. Roué, and B. Lestriez. A comparative study of polyacrylic acid (PAA) and carboxymethyl cellulose (CMC) binders for Si-based electrodes. *Electrochimica Acta*, 258:453–466, dec 2017.

[9] Z. Karkar, D. Guyomard, L. Roué, and B. Lestriez. A comparative study of polyacrylic acid (PAA) and carboxymethyl cellulose (CMC) binders for Si-based electrodes. *Electrochimica Acta*, 258(November):453–466, dec 2017.

[10] Baris Key, Rangeet Bhattacharyya, Mathieu Morcrette, Vincent Seznec, Jean-Marie Tarascon, and Clare P. Grey. Real-Time NMR Investigations of Structural Changes in Silicon Electrodes for Lithium-Ion Batteries. *Journal of the American Chemical Society*, 131(26):9239–9249, jul 2009.

[11] Tae-woo Kwon, Jang Wook Choi, and Ali Coskun. The emerging era of supramolecular polymeric binders in silicon anodes. *Chemical Society Reviews*, 47(6):2145–2164, 2018.

[12] Tae-woo Kwon, You Kyeong Jeong, Inhwa Lee, Taek-Soo Kim, Jang Wook Choi, and Ali Coskun. Systematic Molecular-Level Design of Binders Incorporating Meldrum's Acid for Silicon Anodes in Lithium Rechargeable Batteries. *Advanced Materials*, 26(47):7979–7985, 2014.

[13] Jing Li, R. B. Lewis, and J. R. Dahn. Sodium Carboxymethyl Cellulose. *Electrochemical and Solid-State Letters*, 10(2):A17, 2007.

[14] Wei-Ren Liu, Mo-Hua Yang, Hung-Chun Wu, S. M. Chiao, and Nae-Lih Wu. Enhanced Cycle Life of Si Anode for Li-Ion Batteries by Using Modified Elastomeric Binder. *Electrochemical and Solid-State Letters*, 8(2):A100, 2005.

[15] Xiao Hua Liu, Li Zhong, Shan Huang, Scott X. Mao, Ting Zhu, and Jian Yu Huang. Size-Dependent Fracture of Silicon Nanoparticles During Lithiation. *ACS Nano*, 6(2):1522–1531, feb 2012.

[16] Alexandre Magasinski, Bogdan Zdyrko, Igor Kovalenko, Benjamin Hertzberg, Ruslan Burtovyy, Christopher F Huebner, Thomas F Fuller, Igor Luzinov, and

Gleb Yushin. Toward Efficient Binders for Li-Ion Battery Si-Based Anodes: Polyacrylic Acid. *ACS Applied Materials & Interfaces*, 2(11):3004–3010, nov 2010.

[17] D. Mazouzi, Z. Karkar, C. Reale Hernandez, P. Jimenez Manero, D. Guyomard, L. Roué, and B. Lestriez. Critical roles of binders and formulation at multiscales of silicon-based composite electrodes. *Journal of Power Sources*, 280:533–549, apr 2015.

[18] D. Mazouzi, B. Lestriez, L. Roué, and D. Guyomard. Silicon Composite Electrode with High Capacity and Long Cycle Life. *Electrochemical and Solid-State Letters*, 12(11):A215, 2009.

[19] Cao Cuong Nguyen, Taeho Yoon, Daniel M. Seo, Pradeep Guduru, and Brett L. Lucht. Systematic Investigation of Binders for Silicon Anodes: Interactions of Binder with Silicon Particles and Electrolytes and Effects of Binders on Solid Electrolyte Interphase Formation. *ACS Applied Materials & Interfaces*, 8(19):12211–12220, may 2016.

[20] M. N. Obrovac and L. J. Krause. Reversible Cycling of Crystalline Silicon Powder. *Journal of The Electrochemical Society*, 154(2):A103, 2007.

[21] E Peled and S Menkin. Review-SEI: Past, Present and Future. *Journal of The Electrochemical Society*, 164(7):1703–1719, 2017.

[22] B. Philippe, M. Hahlin, K. Edstro m, T. Gustafsson, H. Siegbahn, and H. Rensmo. Photoelectron Spectroscopy for Lithium Battery Interface Studies. *Journal of the Electrochemical Society*, 163(2):A178–A191, 2015.

[23] Etienne Radvanyi, Eric De Vito, Willy Porcher, and Séverine Jouanneau Si Larbi. An XPS/AES comparative study of the surface behaviour of nano-silicon anodes for Li-ion batteries. *J. Anal. At. Spectrom.*, 29(6):1120–1131, 2014.

[24] Kjell W. Schroder, Hugo Celio, Lauren J. Webb, and Keith J. Stevenson. Examining Solid Electrolyte Interphase Formation on Crystalline Silicon Electrodes: Influence of Electrochemical Preparation and Ambient Exposure Conditions. *The Journal of Physical Chemistry C*, 116(37):19737–19747, sep 2012.

[25] V. A. Sethuraman, A. Nguyen, M. J. Chon, S. P. V. Nadimpalli, H. Wang, D. P. Abraham, A. F. Bower, V. B. Shenoy, and P. R. Guduru. Stress Evolution in Composite Silicon Electrodes during Lithiation/Delithiation. *Journal of The Electrochemical Society*, 160(4):A739–A746, mar 2013.

[26] Vijay A. Sethuraman, Michael J. Chon, Maxwell Shimshak, Venkat Srinivasan, and Pradeep R. Guduru. In situ measurements of stress evolution in silicon thin films during electrochemical lithiation and delithiation. *Journal of Power Sources*, 195(15):5062–5066, 2010.

[27] Feifei Shi, Zhichao Song, Philip N. Ross, Gabor A. Somorjai, Robert O. Ritchie, and Kyriakos Komvopoulos. Failure mechanisms of single-crystal silicon electrodes in lithium-ion batteries. *Nature Communications*, 7(1):11886, dec 2016.

[28] J.-M Tarascon and M Armand. Issues and challenges facing rechargeable lithium batteries. *Nature*, 414(6861):359–367, nov 2001.

[29] A. Tranchot, H. Idrissi, P.-X. Thivel, and L. Roué. Influence of the Si particle size on the mechanical stability of Si-based electrodes evaluated by in-operando dilatometry and acoustic emission. *Journal of Power Sources*, 330:253–260, oct 2016.

[30] Martin Winter and Ralph J. Brodd. What Are Batteries, Fuel Cells, and Supercapacitors? *Chemical Reviews*, 104(10):4245–4270, oct 2004.